STUDY ON CONCEPTS FOR RADAR INTERFEROMETRY FROM SATELLITES FOR OCEAN (AND LAND) APPLICATIONS

Studie zu Konzepten für Radar-Interferometrie über Ozeanen (und Land) im Rahmen zukünftiger Satellitenmissionen

(KoRIOLiS)

SECTION 5: TECHNICAL ISSUES

Marcus Schwäbisch and Robert Siegmund

5.1. Introduction

In this chapter the technical issues related to spaceborne interferometric SAR systems for oceanic applications are studied. The chapter is divided into 3 main sections dealing with hardware issues, data acquisition issues, and data processing issues, respectively. A fourth section summarises the main findings of the investigations.

All calculations and simulations are based on a potential bistatic interferometric system, consisting of a master satellite as illuminator in X- or L-band and one (or more) slave satellite(s) as receivers. Such a configuration is considered as the most likely one to be realised in the near future at the time of preparation of this study (end of the year 2001). The key parameters of this hypothetical system are summarised in Tab. 5-1. They are based on parameters currently discussed for the *TerraSAR* mission.

Table 5-1: Parameters of potential X- and L-band spaceborne systems that may serve as illuminator and receiver for bistatic InSAR experiments

Parameter		X-band	L-band
transmitting system	wavelength [m]	0.031	0.2
	nominal elevation angle (mid-swath) [°]	33.8	33.8
	nominal swath width [km]	30	60
	physical antenna size in elevation [m]	0.7	3.3
	physical antenna size in azimuth [m]	4.8	10
	antenna beamwidth in elevation [°]	2.27	3.5
	antenna beamwidth in azimuth [°]	0.33	1.1
	Doppler bandwidth [Hz]	2600	1400
	Range bandwidth [MHz]	150	25
	Azimuth resolution [m]	2.7	5
	Range resolution [m]	1	6
	maximum PRF [Hz]	6500	2000
	transmitter peak power [kW]	5.9	5.9
	satellite velocity [m/sec]	7000	7000
	orbit altitude [km]	514	514
receiving system	antenna size in elevation [m]	0.7	3.3
	antenna size in azimuth [m]	4.8	10
	mean along-track distance to transmitter [km]	40	40

5.2. Hardware

5.2.1. Platform Specifications

5.2.1.1. Physical Dimensions

The physical dimensions of a spaceborne interferometric SAR system such as size and weight are basically a function of the required system parameters. As an example, a system with high azimuth resolution needs a broader antenna than a low-resolution one, or a system with high power demand needs larger solar panels than a low-power one. On the other hand, physical dimensions define the required launch vehicle's payload capacity, which in turn is the main driver of the launch costs. Therefore, system performance and launch costs can be regarded as reciprocal quantities. A widely used classification of satellite systems in terms of physical dimensions is made according to their weight, as reported in Tab. 5-2, where additionally an order of magnitude for launch costs is quoted.

For a proposed ATI interferometer, physical dimensions will strongly depend on whether the system is an illuminator or a passive receiver only. With respect to the payload weight, receive-only radars may conveniently be operated on a micro satellite, whereas an active SAR needs significantly more payload capacity to be launched with mini or medium satellites. With respect to the system's size, the antenna extent is the defining parameter, setting a lower limit on the size of the carrier's fairing. With respect to the system's weight, a main defining parameter is its envisaged lifetime, which determines the amount of fuel that has to be brought into space for the satellite's attitude and orbit control and occasional manoeuvres. A typical correctional manoeuvre for a medium size satellite burns a few kilogrammes of hydrazine, orbit control for a 10-year lifetime needs in the order of some tens of kilogrammes.

Table 5-2: Classification of satellites

Type	Range of Weights			Range of Launch Costs (order of magnitude, as of 2001)		
nano satellites		<	10 kg		<	1 Mio. US$
micro satellites	10 kg	...	100 kg	1 Mio. US$	...	10 Mio. US$
mini satellites	100 kg	...	500 kg	10 Mio. US$	...	20 Mio. US$
medium satellites	500 kg	...	1000 kg	20 Mio. US$	...	50 Mio. US$
large satellites		>	1000 kg		>	50 Mio. US$

5.2.1.2. Orbit Configuration and Constellation

Orbit design for remote sensing satellites is mainly driven by specific requirements for surface illumination. The main aspects are illumination coverage, repeat cycle, and the system‘s response time:

- *illumination coverage:* for global coverage a (nearly) polar orbit is necessary so that, due to the Earth‘s rotation, the sensor has access to virtually every point on the surface. On the other hand, polar orbits have the disadvantage of higher propellant consumption over orbits with lower inclination since the launch vehicle cannot take advantage of the initial speed provided by the Earth‘s rotation.

  Sun synchronous orbits are not fixed in inertial space, but have the advantage that areas on the surface are always passed at the same (fixed) local time.
- *repeat cycle:* defined as the time period after which the sensor illuminates the same area again under same conditions (such as look angle and look direction). It depends primarily on swath width, satellite

speed (thus, orbit altitude), and illumination coverage. As an example, the ERS satellites needed a 35-day repeat cycle for global coverage at 100 km swath width and 785 km orbit altitude.

- *system's response time:* defined as the maximum time the system needs to illuminate an arbitrarily selected area. For conventional remote sensing systems configured for global coverage with temporally fixed orbit configurations the response time is roughly half of the repeat cycle (due to ascending and descending node passes). However, the response time may be shortened significantly with more widely steerable sensors and lower restrictions regarding the coverage.

Orbit constellation is an important issue for repeat-pass interferometric systems. In order to obtain a cross-track and/or along-track baseline, the orbital planes of the 2 sensors either must differ in celestial longitude (with respect to the ascending node) or in inclination. In any case, the absolute spatial distance of the satellites must not fall below a certain safety threshold, in order to minimise the possibility of satellite collisions or mutual interference by orbital manoeuvres. For the Cartwheel study, this minimum distance was reported as 40 km between the master (illuminating) and slave (receive-only) satellites [*Mittermayer et al.*, 2001].

Bistatic interferometry configurations impose additional requirements on orbit constellation design. The orbit constellations of the recently discussed bistatic experiments *Cartwheel* and *Pendulum* have been investigated in *Mittermayer et al.* [2001] and *Moreira et al.* [2001]. One important issue is to ensure that no mutual interference between expected echoes on the one hand and nadir echoes or directly received signals on the other hand take place. In general, the Cartwheel constellation is considered to be suitable especially for cross-track applications, whereas the Pendulum design in addition is well-suited for along-track applications due to its constant ATI baseline.

5.2.1.3. Platform Position and Attitude Determination

Spaceborne platform motions typically are described giving their position and attitude in a certain reference frame (e.g. earth-fixed earth-centred Cartesian system). Precise tracking of the satellite motions is a stringent requirement for obtaining a high signal-to-noise ratio (SNR) level in both the SAR and InSAR processing. Possible motion errors* have to be corrected by applying a motion compensation, which consists of a modification of the original raw data with respect to their phase value and location in the range/azimuth coordinate frame. In the following paragraphs, first a review of state-of-the-art techniques for satellite tracking is given, followed by a study of effects of inaccurate motion data and uncompensated motion errors related to platform position and attitude.

Tracking Techniques State-of-the-art satellite tracking techniques include the following:

- *GPS:* allows the determination of the satellite's position and velocity.
- *Radar Altimetry:* for measuring the satellite's altitude above the surface.
- *Laser Ranging:* for estimating the satellite's distance to selected reference stations using laser systems.
- *Microwave Ranging:* for estimating the satellite's distance to selected reference stations using microwaves.
- *IRU (Inertial Reference Unit):* measures the relative change of the platform's attitude onboard, using e.g gyro systems.
- *Star Tracker:* used to determine the platform's orientation with respect to inertial space. Star tracker data often are used to compensate for IRU drift in a final solution.

Highly accurate attitude data is only of minor importance for repeat-pass systems since their baseline is only determined by the platform positions. For single-pass cross-track systems, however, platform attitude (especially the roll angle) directly affects the effective baseline.

The satellite position, in general, is measured in a combined solution of the above mentioned techniques. As an example, ERS-1 positional accuracy as derived from laser ranging and radar altimetry techniques resulted in a value of 13 cm [*Scharroo*, 1993].

* Motion errors are defined as deviations of the platform motion from an ideal (linear and uniform) motion

Effects of positional errors Inaccurately measured platform positions lead to a geometric displacement of the radar raw data which in turn results in the following effects:

- geometric displacement of the processed SAR image (if error is systematic). Due to the typically small errors (order of decimeters) compared to the resolution of the system (order of meters) this effect is generally negligible for spaceborne systems.
- defocused SAR image (if error is statistical). Due to the stable and almost linear and uniform satellite trajectories this effect can be neglected.
- phase error in the interferogram. It has to be distinguished between ATI and XTI systems: for XTI, uncompensated cross-track position errors result in an erroneous cross-track baseline, which in turn causes a wrong phase-to-height scaling (cf. Eq. 5-3 below). For ATI, both cross-track and along-track position errors have an impact. A cross-track position error directly transforms into an interferometric phase offset according to the following equation that describes the relation between phase error $\delta\phi$ and line-of-sight position error δR:

$$\delta\phi = \frac{4\pi}{\lambda}\delta R \tag{5-1}$$

  For internally calibrated systems this phase offset will be interpreted as additional interferometric velocity. External calibration (e.g. through use of corner reflectors deployed over land areas) may eliminate the error. Along-track position errors lead to an erroneous along-track baseline, which in turn causes a wrong phase-to-velocity scaling according to Eq. 5-16 below.

  It is important to note that effectively only baseline errors (as opposed to positional errors) affect the interferogram phase, i.e. if both interferometric observations suffer the same positional error no interferometric phase error will result. Furthermore, only the applicable component is relevant, which is the component perpendicular to the look direction for XTI systems and the one along the flight direction for ATI systems.

Effects of attitude errors Inaccurately measured platform attitude leads to the following effects:

- wrong radiometry of the SAR image data after radiometric calibration (caused especially by uncompensated roll angle errors). The radiometric properties of SAR data can be described by the radar equation (e.g. [*Skolnik*, 1990])

$$P_r = \frac{G_t(\theta)\ G_r(\theta)\ \lambda^2\sigma}{(4\pi)^3\ R^4 L} P_t + kTB_eF \tag{5-2}$$

  where P_r = received power
  P_t = transmitted power
  $G_r(\theta)$ = receiving-antenna power gain
  $G_t(\theta)$ = transmitting-antenna power gain
  θ = antenna look angle
  λ = wavelength
  σ = radar cross section
  R = radar-to-target distance
  L = system losses
  k = Boltzmann's constant
  T = receiver temperature
  B_e = equivalent range system bandwidth
  F = receiver noise figure

  Consequently, an uncompensated roll angle error leads to a shift of the antenna gain patterns $G_r(\theta)$ and $G_t(\theta)$, which in turn causes a wrong calculation of the received signal power.
- wrong scaling of the results for single-pass systems due to a wrong orientation of the baseline (which results in a wrong value for the applicable baseline component). For XTI systems especially an uncompensated roll angle error has impact on the phase-to-height transformation of the data. According to Eq.

5-3 phase-to-height scaling is directly determined by the baseline component perpendicular to the look direction $B_\perp$:

$$\delta h = \frac{\lambda R \sin\theta}{4\pi B_\perp} \cdot \delta\phi \tag{5-3}$$

where h = terrain height
λ = wavelength
R = slant range between antenna and object
θ = look angle
$B_\perp$ = baseline component perpendicular to look direction
ϕ = interferometric phase

$B_\perp$ in turn depends on the roll angle α:

$$B_\perp = B\cos(\zeta - \theta + \alpha) \tag{5-4}$$

where B = absolute baseline length, ζ = nominal off-nadir baseline angle, and α = system roll angle.

For ATI systems uncompensated yaw and pitch angle errors lead to a wrong phase-to-velocity scaling since those angles are responsible for the baseline along-track component.

- wrong positioning of the geocoded SAR image (caused mainly by uncompensated yaw angle errors). Yaw angle errors imply a wrong antenna squint angle, which in turn causes an erroneous geometric projection of the data.

5.2.2. Radar System Specifications

The radar system hardware as regarded from the technical point of view includes as key elements the antennas and the microwave part. In the following subsections the relevant design parameters are discussed.

5.2.2.1. Antennas

Design considerations for a SAR antenna have to take into account basically two key parameters, the antenna gain and its radiation pattern. The gain characterises the antenna's ability to concentrate the energy into a narrow angular region. For spaceborne systems, gain values of more than 30 dB are often required in order to achieve the desired SNR. The radiation pattern describes the energy distribution in three-dimensional angular space. It has to be designed in accordance with fundamental system parameters like swath width, azimuth resolution, and ambiguity considerations.

Antenna design includes two main parameters which play key roles in the overall system design regarding performance and costs: the type of antenna used and its size. Both aspects are briefly discussed in the following subsections.

Type Radar antennas are commonly classified into two broad categories, *optical antennas* and *array antennas* [*Skolnik*, 1990]. Among the optical antennas, reflector antennas are often used for SAR systems. Popular array antenna designs for SAR include microstrip phased arrays and slotted waveguides. All of those antenna types have their advantages and disadvantages. As an example, reflector antennas are relatively cost-effective*, whereas phased arrays are more flexible regarding sophisticated operating modes such as ScanSAR (cf. Sec. 5.3.1.3.).

To summarise, selection of the antenna type has to be aligned with system performance requirements on the one hand and cost-effectiveness on the other hand.

* at least as long as they can easily be stored in the launch vehicle's fairing without complicated folding mechanisms

Size The physical size of the antenna has to be designed as trade-off between a variety of parameters. First of all, upper limits are given by constraints imposed by the launch vehicle (i.e. maximum payload weight, size of the cargo bay, etc.). Other (and often contradictory) requirements are coming from the SAR point of view. The antenna height controls the swath width (Eq. 5-5) and range ambiguities (Eq. 5-6), whereas its length controls azimuth resolution (Eq. 5-7)[†], azimuth ambiguities, and PRF selection (Eq. 5-11 below):

$$X_r \simeq \frac{\lambda\, h_{Sat}}{L_{el}\cos^2\theta} \tag{5-5}$$

$$L_{el} > \frac{2\,\lambda\, h_{Sat}\ \tan\theta\, PRF}{c\ \cos\theta} \tag{5-6}$$

$$\Delta x_{az} = \frac{L_{az}}{2} \tag{5-7}$$

where X_r = swath width
λ = wavelength
h_{Sat} = satellite orbital height
L_{el} = antenna height
L_{az} = antenna length
θ = antenna look angle
Δx_{az} = azimuth resolution
PRF = pulse repetition frequency
c = speed of light

Eqs. 5-6 and 5-11 together impose a lower limit on the antenna area A:

$$A = L_{el}L_{az} > \frac{4\,\lambda\, h_{Sat}\, v_{Sat}\tan\theta}{c\ \cos\theta} \tag{5-8}$$

To resume, antenna design is no specific challenge in the overall definition of a spaceborne InSAR for oceanic applications, however, it has to be aligned with major parameters like system performance and costs.

5.2.2.2. Microwave Part

The radar's microwave part includes basic components like local oscillator, chirp generator, high power amplifier, or A/D converter. An InSAR system for oceanic applications has specific requirements with respect to the microwave design. Among the parameters to be delineated the *system noise*, *frequency*, *polarisation*, and *PRF* are most important and discussed in the following.

Phase Noise Low radar phase noise is a basic requirement for interferometric SARs. Phase noise is mainly caused by internal phase jitter of the radar and by thermal noise. With state-of-the-art design and hardware components noise values of a few degrees (rms) regarding the radar phase jitter easily can be achieved. More prominent with respect to the total interferogram noise floor is the effect coming from the thermal noise, which can be evaluated by looking at the SNR that can be achieved over the specific type of terrain (e.g. ocean surface). Following the investigations of *Just & Bamler* [1994], an assumed SNR value of 18 dB (cf. Tab. 5-3 below) already introduces an interferometric phase noise σ_ϕ of around 20° (Fig. 5-1). Such statistical phase noise can be reduced by interferogram multilooking if a loss of geometric resolution can be accepted. In good approximation, the $1/\sqrt{N_L}$-law (N_L = number of independent interferogram looks) can be applied to quantify the noise reduction effect[*]:

$$\sigma_{\phi,N_L} = \frac{\sigma_{\phi,1}}{\sqrt{N_L}} \tag{5-9}$$

Given a reasonable number of looks, N_L = 20, we obtain a multilook noise value of 4.5° resulting from a SNR of 18 dB.

[†] valid for unweighted antenna patterns
[*] cf. Fig. 5-4 and Sec. 5.4.2.2. for additional discussion on noise reduction by interferogram multilooking

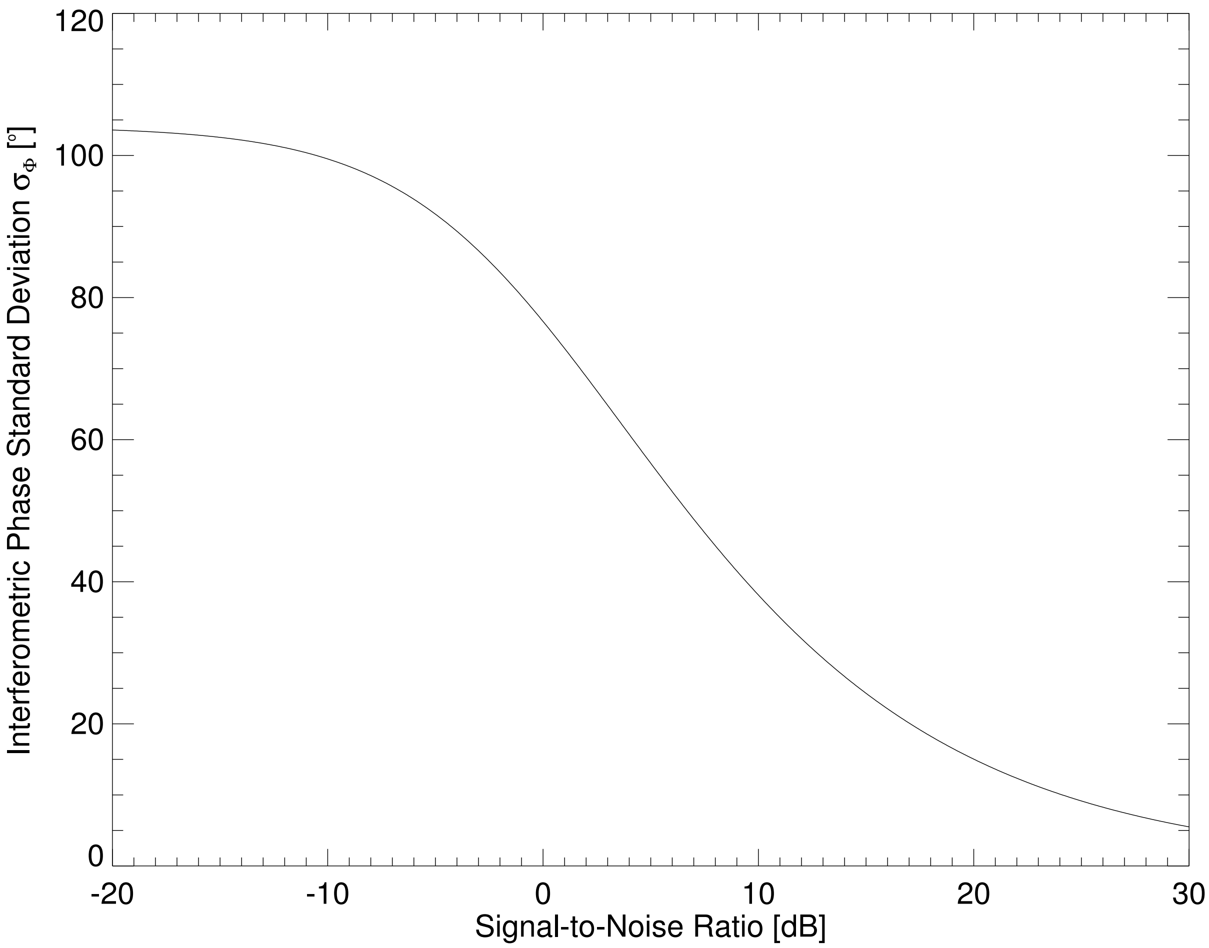

Figure 5-1: Interferometric phase standard deviation versus SNR

Frequency The radar frequency has to be defined by the scientific application and possible technological limitations. For oceanic applications, high frequencies like X-band or even K_u-band are preferable due to their favourable interactions with the water surface. The frequency band has major influence on the type of amplifier and antenna to be used, but there are no principle technological limitations regarding spaceborne X- or K_u-band systems.

Polarisation The preferred polarisation for oceanic applications is VV due to the higher σ^0 values it comes along with (compared to HH- or cross-polarised systems). The type of polarisation has an impact on the antenna design, but there is no technological limitation regarding the construction of vertically polarised antennas.

Bandwidth The bandwidth B_r is driven by the user's requirement for geometric resolution in range, Δx_r:

$$\Delta x_r = \frac{c}{2\,B_r} \tag{5-10}$$

where c = speed of light. A limitation for B_r usually lies in the capability of handling the resulting data rate rather than in any technological constraints. However, for oceanic applications such as current measurements rather low resolution systems are required (e.g. 50 m). But even for the considered high resolution case (1 m for X-band, cf. Tab. 5-1) a bandwidth of only 150 MHz is required, a value which is easily accomplishable for a spaceborne SAR.

Pulse Repetition Frequency The pulse repetition frequency (PRF) is determined by the Nyquist sampling theorem which sets a lower limit on the sampling of the (Doppler-broadened) radar echoes:

$$PRF > \frac{2\, v_{Sat}}{L_{az}} \tag{5-11}$$

where L_{az} = antenna size in azimuth. Recalling that L_{az} is directly related to the system's azimuth resolution (Eq. 5-7) and assuming a value of 2.7 m for Δx_{az} (X-band case, cf. Tab. 5-1), a minimum PRF of around 2.6 kHz is required. Upper PRF limits are often given again by the data rate handling and by the range ambiguity condition (Eq. 5-6). The latter restriction defines a maximum PRF value of 8.2 kHz for the discussed X-band system. In general, values in that order of magnitude are no constraint from the hardware point of view. From the users point of view, high PRF values are always preferable since they result in more signal power and hence, a better SNR, in the processed image. Additionally worth to note is that the PRF has to be tuned so that echo reception fits into the time gaps of subsequent pulse transmissions.

Power Power is a main constraint for all active radar systems and is usually limited by the available raw power on the spacecraft and also the type of amplifier used. The received echo power depends on the transmitted power and a number of factors that attenuate the signal. Tab. 5-3 illustrates the total power budget for the potential X- and L-band systems of Tab. 5-1 in terms of the SNR:

$$SNR = \frac{P_r}{P_n} = \frac{P_r}{kTB_eF} \tag{5-12}$$

Evaluating Eqs. 5-12 and 5-2 and the following expression for the radar cross section σ [*Moreira*, 1992]

$$\sigma = \sigma^0\ \Delta E\ R\ \theta_{az} \tag{5-13}$$

where σ^0 = normalised radar cross section, and ΔE = projected pulse length, we find a total SNR value of 17.9 dB for X-band and 26.3 dB for L-band. Note, that this evaluation is based on a σ^0 value of -10 dB, which may be a typical value for certain circumstances, but may differ significantly for other conditions (incidence angle, wind speed). Furthermore, a monostatic system with $G_t = G_r$ was assumed, for bistatic configurations that are currently under discussion a lower SNR value (caused by a smaller rx antenna) may follow.

Table 5-3: Total power budget for potential X- and L-band systems

Parameter		X-band		L-band	
		physical units	dB	physical units	dB
transmitted power	P_t	5.9 kW	37.7	5.9 kW	37.7
transmitting-antenna gain	G_t	45.7 dB	45.7	38 dB	38.0
receiving-antenna gain	G_r	45.7 dB	45.7	38 dB	38.0
wavelength	λ^2	λ = 0.031 m	-30.1	λ = 0.2 m	-14.0
normalised radar cross section	σ^0	-10 dB	-10.0	-10 dB	-10.0
radar-to-target distance	$1/(4\pi\ R)^3$	R = 619 km	-206.7	R = 619 km	-206.7
equivalent range system bandwidth	$1/B_e$	B_e = 150 MHz	-81.8	B_e = 25 MHz	-74.0
Boltzmann's constant	$1/k$	k = 1.38·10^{-23}	228.6	k = 1.38·10^{-23}	228.6
receiver temperature	$1/T$	T = 300 K	-24.8	T = 300 K	-24.8
receiver noise figure	$1/F$	-4.3 dB	-4.3	-4.3 dB	-4.3
ohmic losses	$1/L$	-2.2 dB	-2.2	-2.2 dB	-2.2
projected pulse length	ΔE	17800 m	42.5	5300 m	37.2
antenna beamwidth in azimuth	θ_{az}	0.33°	-22.4	1.1°	-17.2
SNR			17.9		26.3

5.3. Data Acquisition

In this chapter issues related to the data acquisition of spaceborne interferometric SARs for oceanic applications are discussed. The chapter is subdivided into a *SAR Acquisition Mode* section and an *Interferometry Mode* section.

5.3.1. SAR Acquisition Mode

The three common SAR acquisition modes are illustrated in Fig. 5-2: Stripmap SAR, Spotlight SAR, and ScanSAR. In the following, their advantages, disadvantages, and suitability for interferometric applications are reviewed.

5.3.1.1. Stripmap SAR

Stripmap SAR is the most common type of data acquisition for spaceborne systems. Its advantage is the mapping of contiguous strips which enables the coverage of extended areas with one pass. Main disadvantages are the limited swath width and azimuth resolution. The azimuth resolution Δx_{az} of a stripmap system is defined by the antenna opening angle θ_{az} in azimuth via

$$\Delta x_{az} = \frac{\lambda}{2\,\theta_{az}} \tag{5-14}$$

Stripmap SAR has been successfully applied in numerous InSAR experiments both in cross-track and along-track mode. The only spaceborne ATI experiment at the time being has been conducted with data from the SRTM mission*, first results are reported in *Bao et al.* [2001].

5.3.1.2. Spotlight SAR

A Spotlight SAR steers the antenna beam to continuously illuminate a certain region on ground much longer than in the Stripmap case [*Carrara et al.*, 1995]. As a result, the azimuth bandwidth becomes larger, which hence may be exploited to increase the azimuth resolution. However, for oceanic applications the ocean coherence time puts a constraint on the length of the SAR integration time so that an increase of the azimuth resolution is not always advantageous. But a further feature of the Spotlight mode, which is the fact that objects are observed under a wider range of aspect angles, can be utilised especially for ATI applications. It offers the possibility to measure different components of the surface current using only a single pass (in case of a spotlight single-pass interferometry configuration). To this purpose the total azimuth bandwidth is divided into different (e.g. two) non-overlapping parts which are processed separately with their individual optimum Doppler centroid values so that the resulting images represent observations from two different aspect angles (Fig. 5-3). A spotlight system operated in that way provides data similar to a Dual-Beam ATI configuration (cf. Sec. 5.3.2.4.).

5.3.1.3. ScanSAR

ScanSAR systems image several subswaths parallel to the flight direction by steering the antenna beam in elevation [*Moore et al.*, 1981]. This mode of operation results in a much wider swath at the expense of a decrease in azimuth resolution. However, due to the switching scenario of the beams interferometric observations become more complicated compared to stripmap systems and especially for repeat-pass configurations [*Bamler et al.*, 1999]. Only if there is sufficient synchronisation of the observations with respect to the aspect angle, the spectral properties of the data allow a coherent interferometric combination of the datasets. Due to this inherent limitation ScanSAR is not recommended for operational spaceborne interferometric data acquisition unless the antenna pointing can be controlled as in single-pass systems like SRTM (C-band).

* In particular, SRTM up to now was the only spaceborne single-pass InSAR experiment

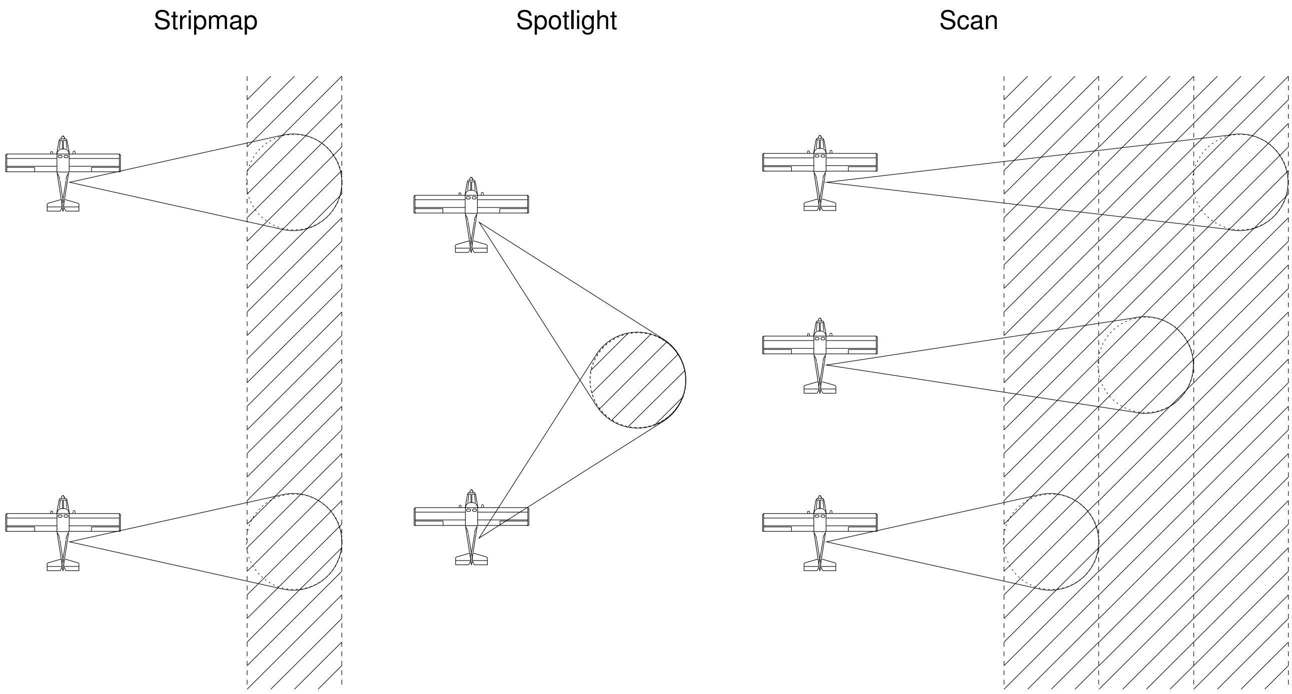

Figure 5-2: SAR acquisition modes, illustrated with an airborne SAR system

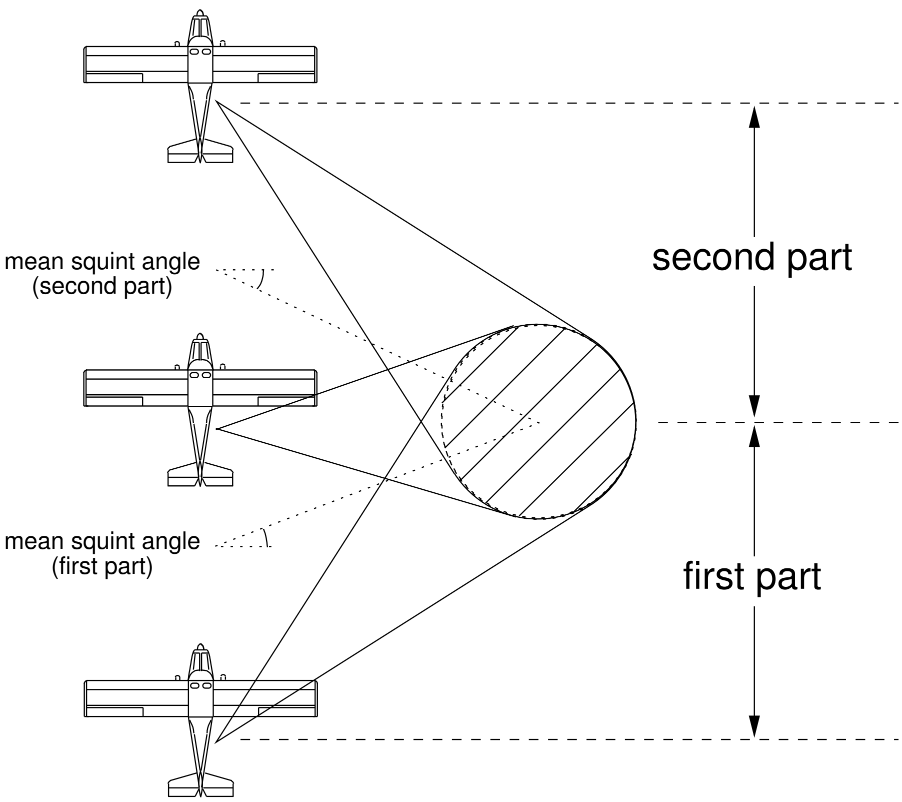

Figure 5-3: Spotlight acquisition divided into two parts with different mean squint angles

5.3.2. Interferometry Mode

Interferometric data can be collected in different acquisition modes and with different parameters. In the following sections general parameters like swath width, baseline, or look angle are discussed and the interferometer configurations *ATI*, *Combined ATI/XTI*, and *Dual-Beam ATI* are investigated.

5.3.2.1. General Parameters

Baseline The (spatial) baseline of an interferometer is defined as the physical displacement of the antennas illuminating the ground. It determines its sensitivity of measuring the desired quantity. For XTI systems, the height is inversely proportional to the baseline component orthogonal to the look direction according to Eq. 5-3, i.e. the larger the baseline, the more sensitive the instrument. On the other hand, increasing baseline values imply a loss of geometric resolution in the interferogram since the usable overlapping spectral portion of the two SAR datasets reduces with increasing baseline [*Gatelli et al.*, 1994]. Accordingly, the length of an XTI baseline is designed as a trade-off between sensitivity (Eq. 5-3) and resolution (Eq. 5-10). The critical baseline value $B_{\perp_{crit}}$ beyond which all spectral overlap is lost, is dependent on the system's frequency bandwidth in range B_r and the wavelength λ according to

$$B_{\perp_{crit}} = \frac{B_r\,\lambda\,R\,\tan\theta_i}{c} \tag{5-15}$$

where R = range distance between antenna and object, θ_i = local incidence angle, c = speed of light. Eq. 5-15 holds for systems where the effective signal path difference is twice the radar-to-target distance difference (e.g. if both antennas transmit and receive separately). If both rx antennas are differing from the tx antenna (which is the case for the discussed Cartwheel configuration), the effective baseline is only half of the physical one, subsequently reducing the sensitivity by a factor of 2. For the bistatic system assumed in Tab. 5-1 we get a value $B_{\perp_{crit}}$ of around 12.8 km for X-band (13.8 km for L-band).

For ATI systems, the baseline along the flight direction determines the sensitivity to measure velocities according to

$$\delta v = -\frac{v_{Sat}\lambda}{4\pi B_{\|}}\cdot\delta\phi \tag{5-16}$$

where v = moving object's velocity, λ = wavelength, v_{Sat} = platform velocity, $B_{\|}$ = baseline component along the flight direction, and ϕ = interferometric phase. Again, Eq. 5-16 holds only for systems with both antennas transmitting and receiving, the effective baseline is halved if the observation is carried out in bistatic mode. The length of an ATI baseline is designed as a trade-off between sensitivity and data coherence since coherence drops with increasing time lags due to changes of the ocean surface. The coherence degradation caused by ocean surface decorrelation can be expressed by the following equation:

$$\gamma(t) = \gamma_0\,\exp\left(-\frac{t}{\tau_s}\right) \tag{5-17}$$

where γ_0 = data coherence for zero time lag, τ_s = ocean decorrelation time. τ_s depends on a variety of parameters like wind speed or radar wavelength. Typical values are 15 msec for X-band and 50 msec for L-band. The drawback of a coherence loss is the thereby induced phase noise. Fig. 5-4 illustrates the dependence between interferometric phase noise and data coherence, which in turn is dependent on the number of interferometric looks N_L that are used to form the interferogram. For a reasonable value N_L = 20 (note that the geometric resolution drops with increasing N_L) the phase standard deviation increases rapidly for coherence values below $\simeq$ 0.4.

The aforementioned values along with the system parameters of Tab. 5-1 allow the evaluation of the useful ATI baseline range. The maximum (critical) baseline follows from the satellite speed and the decorrelation time and reaches a value of 210 m for X-band, resp. 700 m for L-band. The minimum value for $B_{\|}$ of course being 0, the optimum value is determined by the user's velocity resolution requirements. Assuming a phase noise of 4.5° caused by thermal noise only (Sec. 5.2.2.2.) and a desired resolution of 0.1 m/sec, a preferred baseline of 27 m for X-band (175 m for L-band, assuming identical thermal noise) would result (Eq. 5-16, bistatic case!). However, any timelag causes additional phase noise (due to surface decorrelation), which in turn decreases the achievable resolution. The other way round, the velocity resolution can be calculated on the basis of a

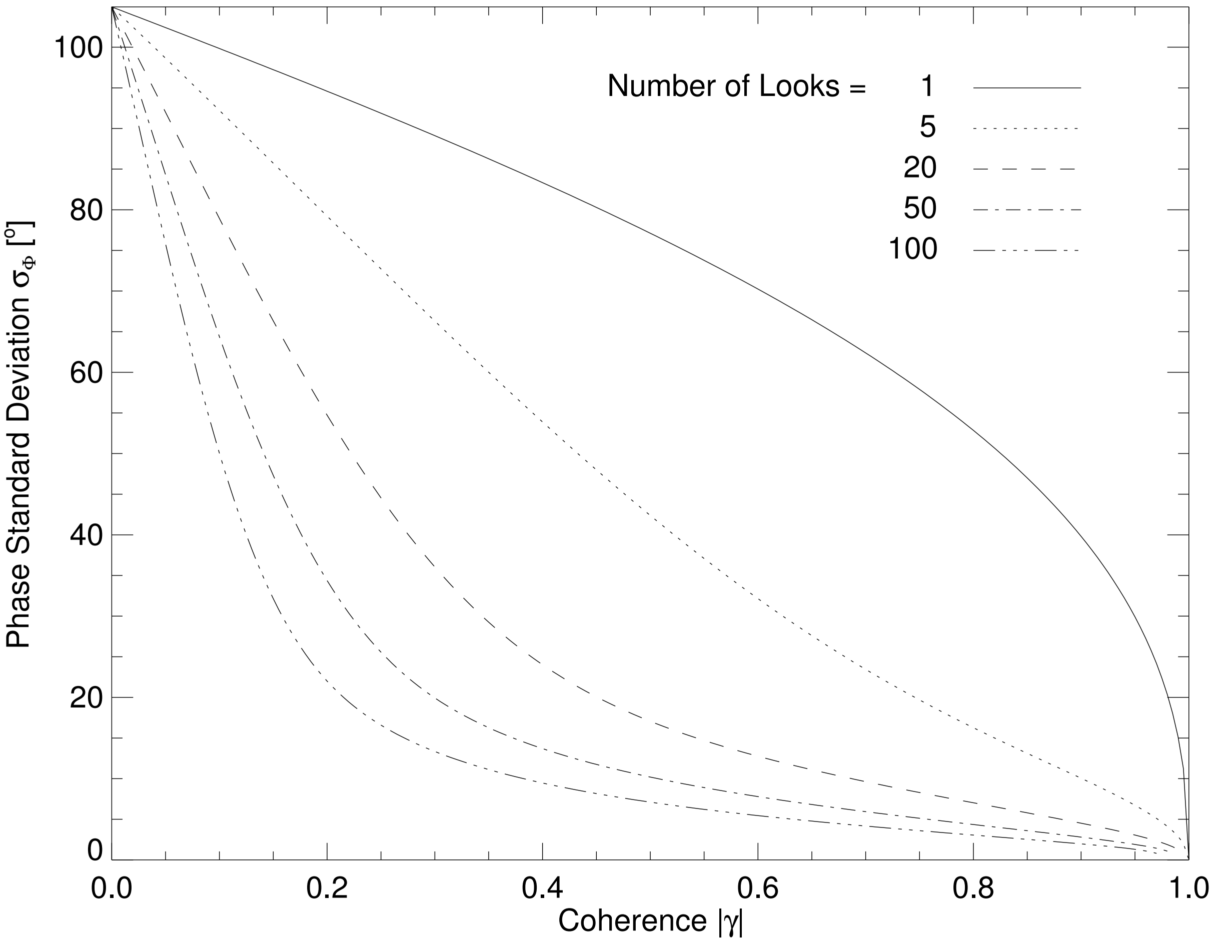

Figure 5-4: Interferometric phase standard deviation as a function of data coherence for different numbers of interferometric looks

timelag that guarantees sufficient data coherence. Starting with an acceptable coherence drop to 0.5 we get a timelag of around 0.7$\cdot\tau_s$, leading to spatial baselines of 147 m for X-band and 490 m for L-band (equivalent to timelags of 0.011 sec and 0.035 sec, respectively). Coherence 0.5 gives an additional phase noise of around 10°, so together with 4.5° phase noise resulting from 18 dB SNR (Sec. 5.2.2.2.) we obtain an overall noise figure of $\simeq$ 11° for X-band. Inserting those values into Eq. 5-16, a velocity resolution of 0.05 m/sec follows. Respective calculation for L-band (again on the basis of equal thermal noise) yields a resolution of 0.09 m/sec.

Fig. 5-5 gives an impression of the interdependency between sensitivity, data coherence, and ATI timelag. In the upper row interferometric phase (left) and coherence (right) for 6 msec timelag is shown, the lower part depicts analogue images of the same area, but acquired with 3 msec timelag. It becomes obvious that on the one hand coherence drops significantly with increasing timelag, yet on the other hand at the same time the sensitivity rises substantially. The data stem from an airborne X-band ATI experiment over the Atlantic Ocean near the city of Gijon, Spain.

Look Angle The instrument's look angle, and correspondingly the wave's incidence angle, affects the kind of scattering on the ocean surface. Typical mean incidence angles (at least for land applications) lie around 45° in order to counterbalance effects of shadow and layover. However, for satellite systems this value is rather high due to power constraints since the radar-to-target distance R_0 enters the radar equation (Eq. 5-2) with the power of 4. Besides the power loss for increasing range distances the backscatter properties of ocean surfaces put another limit on the antenna look angle. The normalised backscatter cross section σ^0 strongly

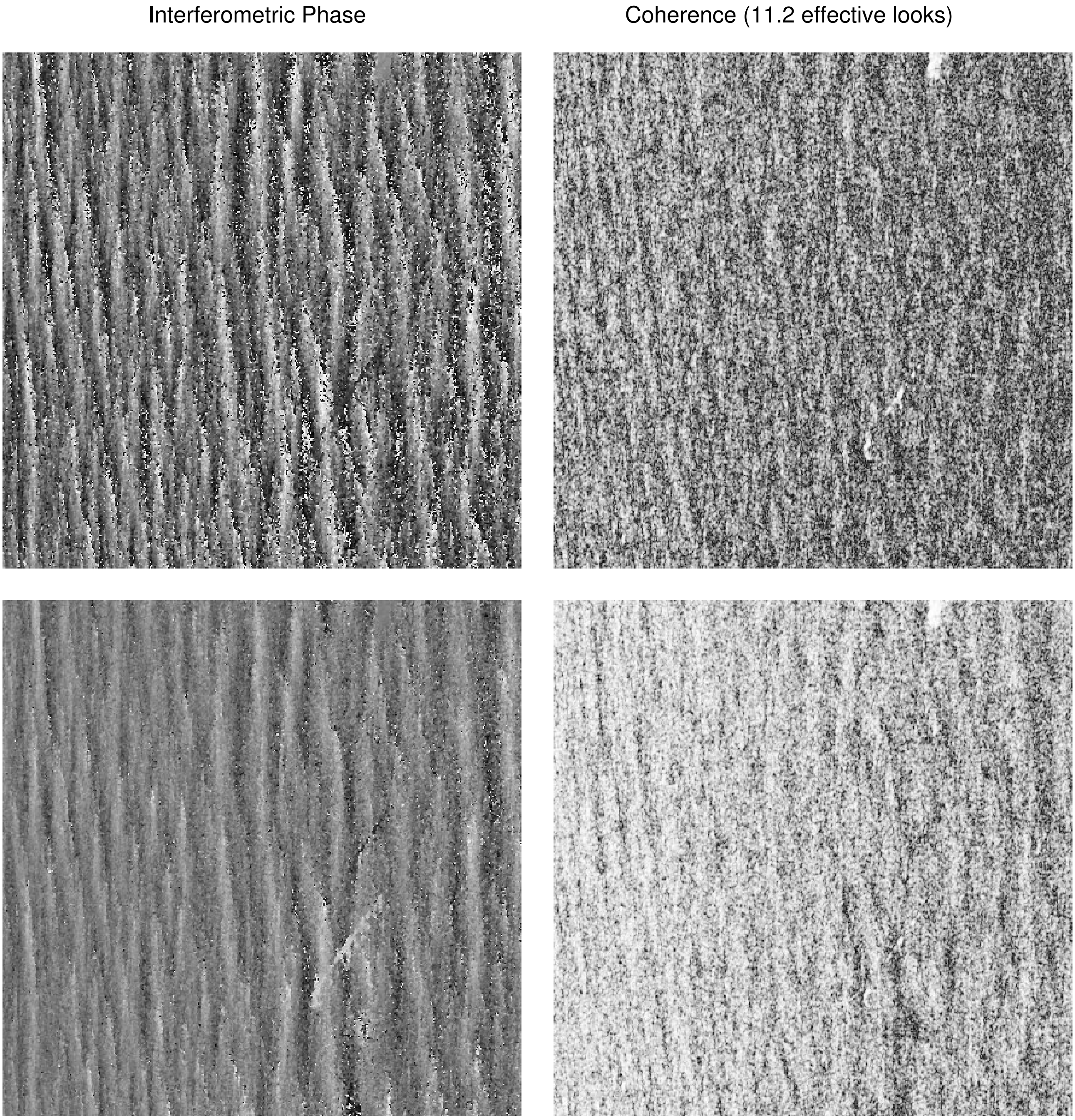

Figure 5-5: Interferometric phase (left column) and coherence (right column) for timelags of 6 msec (upper part) and 3 msec (lower part), respectively. (Source: airborne X-band data acquired with AeS-1 over the Atlantic Ocean near the city of Gijon, Spain.)

depends on the incidence angle, as depicted in Fig. 5-6 which shows the behaviour of σ^0 for different wind speeds and a radar frequency of 13.96 GHz (from *Elachi* [1988]).

An example with real data is shown in Fig. 5-7, which has been acquired with the airborne SAR AeS-1 over the Atlantic Ocean near the city of Gijon, Spain. In the upper part, the radiometrically calibrated amplitude is depicted, the diagram below shows the cross section decrease with incidence angle (averaged over all rangelines). The noise-equivalent σ^0 (NESZ) for this dataset has been estimated to $\simeq$ -16 dB, so that for an

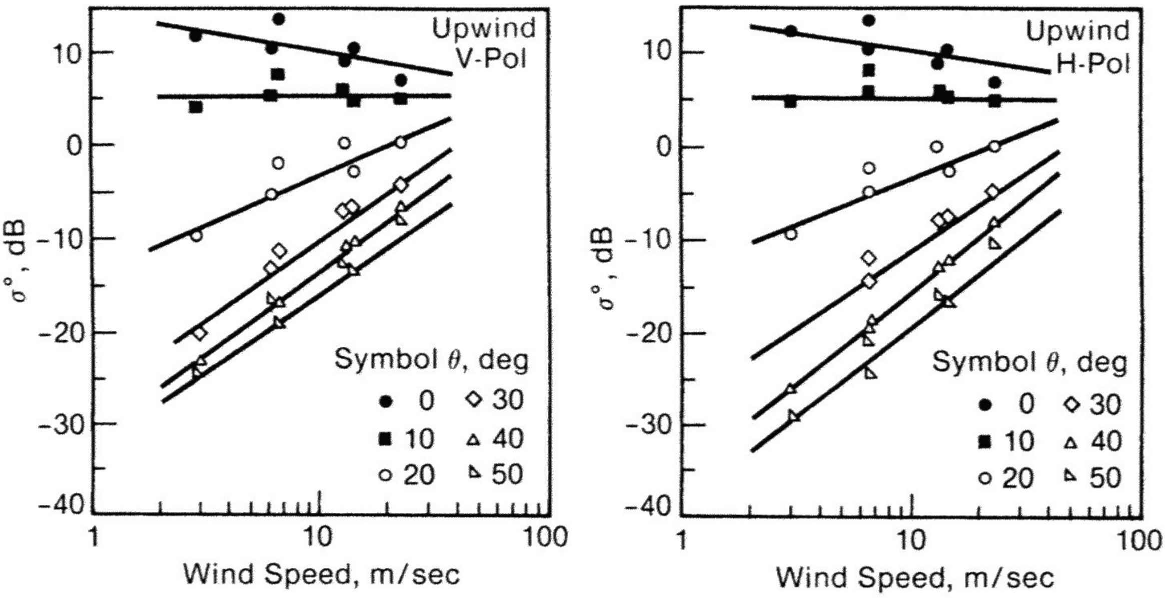

Figure 5-6: Backscatter cross section of the ocean surface as a function of windspeed for different incidence angles θ and radar frequency 13.96 GHz (from Elachi *[1988]); left: V-polarisation, right: H-polarisation*

incidence angle of 30° we obtain a SNR of around 11 dB. This value is close to the expected value reported in Tab. 5-3 so that Fig. 5-7 gives a realistic impression of the expected image quality of the discussed bistatic system.

Swath Width The swath width is normally determined by user requirements on the one hand and system constraints on the other hand. A wide swath, which often is preferred by the user, collides with system power limitations, usable incidence angle ranges (controlled by scattering mechanisms), and system design parameters (antenna design, range and azimuth ambiguities, etc.).

Doppler Properties Each radar echo undergoes a Doppler frequency shift f_D related to the relative velocity v_{rel} between sensor and target:

$$f_D = \frac{2\,\vec{v}_{rel} \cdot \vec{e}_R}{\lambda} \tag{5-18}$$

where $\vec{e}_R$ = unity vector in sensor-to-target direction. Due to the finite and non-zero antenna opening angle in azimuth a certain spectrum of Doppler frequencies is observed with each transmitted pulse. An overlap of the Doppler spectra of the 2 interferometric datasets is a prerequisite for achieving data coherence. Spectral mismatch is caused by different antenna squint angles and introduces a loss of azimuth bandwidth (and hence, resolution). Additionally, phase noise is generated by the non-overlapping parts of the azimuth spectra, which should be removed by proper bandpass filtering [*Schwäbisch & Geudtner*, 1995].

In single-pass systems, the spectra's overlap typically is guaranteed due to the fact that the antennas are mounted on the platform with identical viewing angles. In repeat-pass systems, however, the overlap depends on the system's capabilities to maintain a certain antenna orientation. Particularly, bistatic ATI systems such as Cartwheel suffer from a spectral mismatch: due to the along-track separation of the antennas in combination with a single transmitting antenna, an aspect angle difference over the entire aperture is present*. From Eq.

*unless antenna orientation is controlled for each sensor separately according to the actual baseline. However, such a procedure requires extensive attitude control, which is undesirable e.g. from the point of view of fuel consumption.

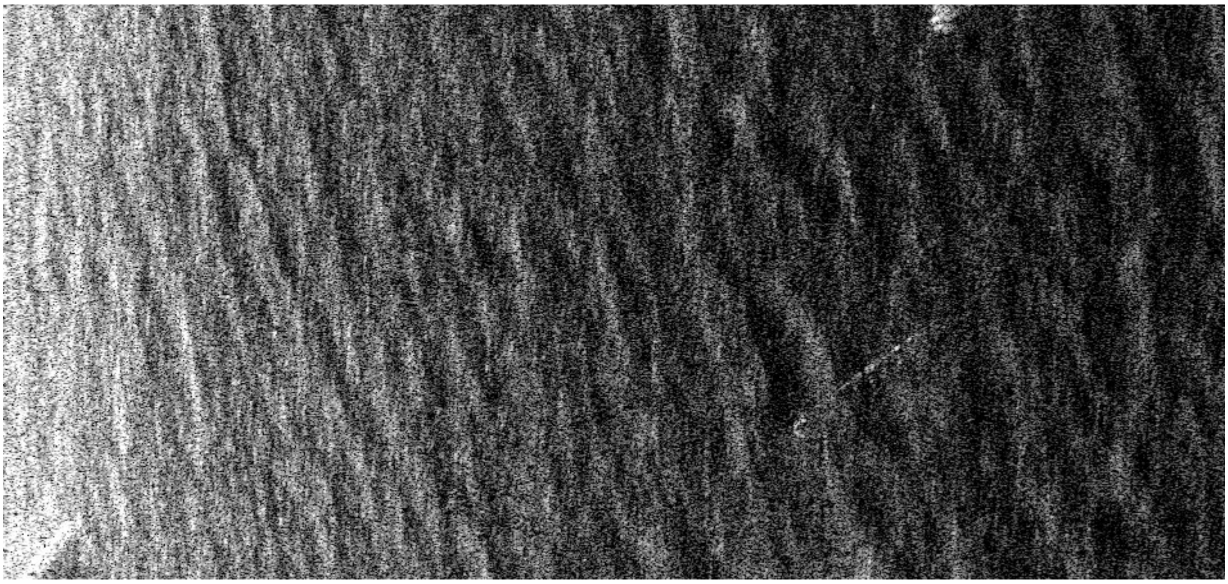

(a)

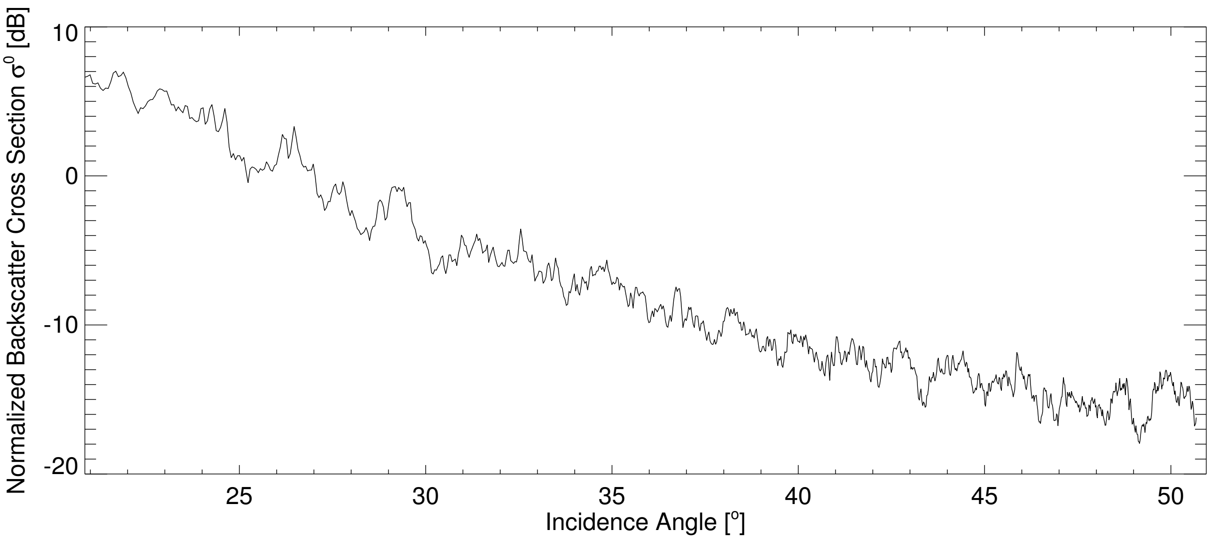

(b)

Figure 5-7: Radiometrically calibrated airborne SAR image of the ocean surface, Atlantic Ocean near Gijon (Spain): (a) Amplitude (b) Normalised backscatter cross section σ^0 as a function of the incidence angle, averaged over all rangelines from (a)

5-18 the Doppler frequency difference Δf_D can be evaluated according to the following relation:

$$\begin{aligned} \Delta f_D &= \frac{2\,\vec{v}_{rel}\cdot\vec{R}}{\lambda\,R} - \frac{2\,\vec{v}_{rel}\cdot\left(\vec{R}+\frac{\vec{B}}{2}\right)}{\lambda\left(R+\frac{B}{2}\right)} \\ &\simeq -\frac{\vec{v}_{rel}\cdot\vec{B}}{\lambda\,R} \end{aligned} \tag{5-19}$$

Note that only half of the spatial baseline enters the equation due to the fact that the transmitting antenna is the same for both signals. The spectral mismatch can be evaluated assuming the spatial baselines 147 m (for X-band) and 490 m (for L-band) above, yielding a frequency difference of 54 Hz (for X-band) and 28 Hz (for L-band), respectively. Both values are negligibly small when compared to the Doppler bandwidth (2600 Hz for X-band, 1400 Hz for L-band).

Additionally, the absolute mean Doppler shift for echoes of bistatic configurations have to be considered since significant Doppler values impose more stringent requirements on image processing (especially image co-registration, cf. Sec. 5.4.2.1. below). For bistatic observations, Eq. 5-18 transforms to

$$\begin{aligned} f_D &= \frac{\vec{v}_{rel,tx} \cdot \vec{e}_{R,tx}}{\lambda} + \frac{\vec{v}_{rel,rx} \cdot \vec{e}_{R,rx}}{\lambda} \\ &\simeq \frac{v_{rel}}{\lambda}(\sin\varphi_{tx} + \sin\varphi_{rx}) \\ &\simeq \frac{v_{rel}}{\lambda}\arctan\left(\frac{D_{bistatic}}{R}\right) \end{aligned} \tag{5-20}$$

where indices tx, rx indicate transmitting and receiving antenna, respectively, φ_i denotes the corresponding antenna squint angles, $D_{bistatic}$ is the (along-track) distance between transmitting and receiving sensor, and pulse transmission perpendicular to the flight direction is assumed. For the considered bistatic configuration a mean Doppler centroid value of around 14.6 kHz for X-band (2.3 kHz for L-band) follows. Using Eq. 5-29 and replacing squint angle with Doppler frequency (cf. Eq. 5-18), a co-registration accuracy requirement of 0.4 resolution cells follows for keeping the phase bias below 5°.

5.3.2.2. ATI

The ATI mode is characterised by a separation of the antennas along the flight track, establishing a time lag (or temporal baseline) between both observations. From the technical point of view, spaceborne ATI for oceanic applications gives rise to a number of requirements and limitations. Most of them have already been investigated in previous sections, the following paragraphs resume the key issues.

- *Baseline:* a crucial issue is to find an optimum baseline as a trade-off between sufficient interferometer sensitivity (provided by long time lags) and sufficient data coherence (provided by short time lags) (cf. Sec. 5.3.2.1.).
- *Satellite distance:* if ATI is realised in repeat-pass mode, the spatial distance of the satellites spanning the ATI baseline has to meet certain requirements in order to avoid risk of collision and mutual interference (cf. Sec. 5.2.1.2.).
- *Doppler spectra overlap:* for bistatic ATI observations like Cartwheel a Doppler spectra mismatch between the receiving sensors occur, caused by their difference in observation angles.

5.3.2.3. Combined ATI/XTI

Originally, satellite radar interferometry has been used exclusively in XTI mode for terrain height estimation due to the lack of sensor constellations that provide sufficiently short timelags. The principal capability of establishing an ATI system in space also leads to the possibility of using a combined approach. This technique is promising especially for simultaneous determination of oceanographic parameters such as wind fields and topography in coastal areas [*Greidanus et al.*, 1999a,b]. Combined ATI/XTI is described by the following characteristics:

- *Baseline:* general satellite-based interferometry always dealt with baselines consisting of cross-track components only, again due to the absence of interferometer constellations that provided sufficiently short ATI timelags. For oceanic applications an optimum configuration for combined ATI and XTI imaging may be desired. This combined baseline consists of temporal and spatial components. The temporal component is given by the ATI baseline, while the XTI baseline forms the spatial component, cf. Sec. 5.3.2.1.. The first spaceborne experiment with combined ATI/XTI components has been the SRTM mission where a small ATI component was existing [*Bao et al.*, 2001], however, this ATI component was present by accident only and was far too small for reasonable oceanic investigations.
- *Baseline Length:* as pointed out in the previous section 5.3.2.1. the length of the temporal baseline is crucial for decorrelation effects. An optimum baseline can be calculated for an expected surface velocity using the ocean coherence time. Analogous to Sec. 5.3.2.1. the spatial component represents the cross-track component. Limitations and sensitivity are the same as in pure XTI.

- *Combined ATI/XTI Phase:* the resulting phase of a combined ATI/XTI acquisition contains topographic and motion effects. As compared to pure ATI or XTI, the phase components resulting from surface motion and terrain variation add together according to:

$$\phi = \phi_{ATI} - \phi_{XTI} \tag{5-21}$$

  Obviously, the resulting phase is ambiguous, and the influence of topography and surface motion has to be separated (cf. Sec. 5.4.3. below).

  Contributions of surface motions on the interferometric phase include the phase velocity of the Bragg waves, orbital motions of the swell (both depending on the used wavelength), the surface current of the water, and the drift that results from wind over the water surface. On the other hand, topographic effects on the phase over ocean areas result from very long waves and the topography of the swell.

  As in pure SAR mode, due to the motion of the scatterer on an ocean surface its original position is displaced according to its velocity in the antenna line-of-sight, which causes an additional Doppler frequency contribution equivalent to a displacement in azimuth (cf. Sec. 5.4.1.4., Eqs. 5-27 and 5-28 below). In combined ATI/XTI and especially for interpretation and derivation of wave fields this is an important issue that has to be considered [*Schulz-Stellenfleth et al.*, 2001].

  An additional phase shift is induced by potential misregistration of the datasets in case of squinted geometry (cf. Sec. 5.4.2.1.). Such a misregistration may be caused by the effect of a moving scatterer in case of a non-zero cross-track baseline component. The thereby induced different viewing angles result in different radial velocity components in antenna line-of-sight, thus causing a different additional Doppler shift and hence, a different displacement (cf. Eqs. 5-27 and 5-28 below). In presence of squint, this misregistration leads to a phase bias given by Eq. 5-29.

5.3.2.4. Dual-Beam ATI

Dual-Beam ATI has first been introduced by *Frasier & Camps* [2001]. The two antennas used for ATI work in dual-beam mode, one beam looking forward (forward beam) and one looking backward (aft beam) (Fig. 5-8). The two forward beam datasets and the two aft beam datasets are combined to interferograms, respectively, yielding two interferometric velocity fields representing different radial components of the two-dimensional vector field. The main benefit of this design is that this two-dimensional current field is obtained with a single pass only. On the other hand, drawbacks especially for spaceborne systems are present:

- the use of nominally sidelooking antennas radiating squinted beams implies polarisation mixing in the received signal for high squint angles (> 30°) [*Frasier & Camps*, 2001].

- alternatively using two different antennas physically oriented along the squint directions implies additional hardware effort and especially weight, which is undesirable for spaceborne systems.

- squint processing implies high demands on SAR as well as interferometric processing (cf. Sections 5.4.1.3. and 5.4.2.1.).

5.4. Data Processing

In this section issues related to the data processing of spaceborne InSAR data for oceanic applications are studied. The following subsections deal with SAR processing, InSAR processing, separation of ATI and XTI contributions, and geocoding. A detailed description of general issues of SAR and InSAR data processing can be found e.g. in *Elachi* [1988]; *Curlander & McDonough* [1991]; *Carrara et al.* [1995]; *Soumekh* [1999]; *Franceschetti & Lanari* [1999].

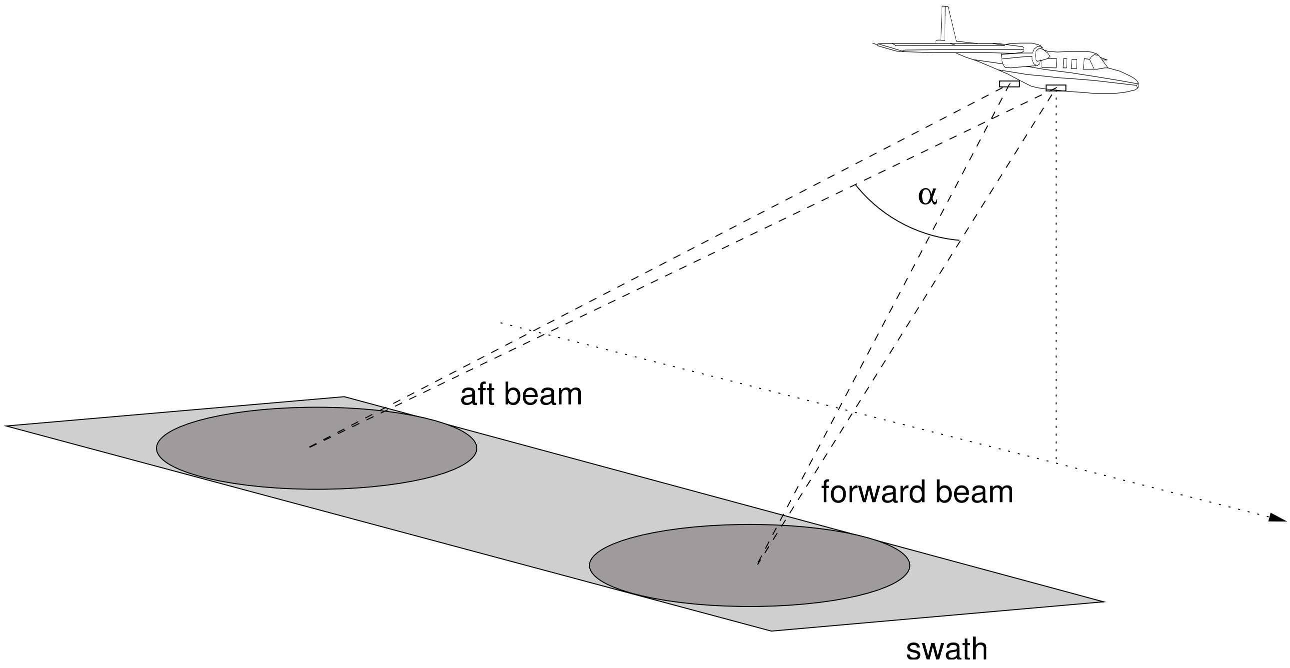

Figure 5-8: Principle of Dual-Beam ATI, illustrated with an airborne InSAR system

5.4.1. SAR Processing

5.4.1.1. Focusing

In order to exploit the full system resolution, high-resolution SAR image formation requires pulse compression in the range and azimuth domain, a process which is also called signal data *focusing*. In particular, azimuth compression is demanding since range and azimuth coordinates are coupled in the signal impulse response, an effect called *range cell migration*. Among the SAR focusing techniques currently mainly 3 algorithms are in use: *Range/Doppler*, ω-*k*, and *Chirp Scaling*. The *Range/Doppler* algorithm is the most widely used technique and is suitable for most of the applications, including interferometric processing which requires phase-preserving focusing. However, one drawback of this technique is that for high squint angles the image quality suffers a slight defocusing caused by range and azimuth coupling during range migration correction [*Jin & Wu*, 1984]. Although this effect can be minimised by a technique called *secondary range compression*, the decrease in computational efficiency is significant. The ω-*k* technique avoids the range defocusing effect and is computationally efficient at the same time. However, it still needs an interpolation operation (*Stolt interpolation*) which can degrade its phase preserving properties. The *Chirp Scaling* algorithm allows efficient high precision SAR processing without any interpolation step during focusing [*Raney et al.*, 1994].

5.4.1.2. Motion Compensation

Classical motion compensation, which is applied to correct for deviations of the real platform motion from a linear and uniform one, typically is not required for spaceborne systems due to their stable and homogeneous motion. In single-pass configurations, however, problems may arise due to motions of the phase centre of the antennas unless both of them are mounted rigidly to the spacecraft body, thus impeding potential vibrations. As an example, the SRTM interferometer design with its 60 m boom for the slave antenna experienced oscillations at the end of the mast, leading to phase errors in the interferogram [*Eineder et al.*, 2000].

In addition, inaccurately measured motion data (that may be regarded as motion errors), as discussed in Section 5.2.1.3., may have a strong impact on the data quality and therefore has to be avoided by the use of precise tracking mechanisms. Especially baseline uncertainties, which may result from erroneous positioning of repeat-pass systems, directly affect the measurement accuracy of the interferometer (Eqs. 5-15, 5-16).

5.4.1.3. Properties of Squint Mode Acquisitions

Data acquired in squint mode hold particular signal properties related to the Doppler frequency shift. Two main effects occur [*Davidson & Cumming*, 1997]:

- the Doppler centroid frequency f_{DC} becomes a function of range (and elevation angle). This is undesirable since processing effort increases and, more important, azimuth ambiguities may occur if f_{DC} variations are bigger than the difference between PRF and PBW (processed azimuth bandwidth).
- the squinted azimuth beamwidth (and hence the azimuth bandwidth) becomes a function of range (and elevation angle). This is undesirable since the fundamental SAR property that azimuth bandwidth is independent of range is violated.

In order to minimise the aforementioned effects the antenna pitch and yaw angles with respect to the desired squint angle have to be adjusted [*Davidson & Cumming*, 1997]. For a nominal elevation angle ρ_n and desired squint φ_d the optimum pitch and yaw values are given by

$$\psi = \arctan(\sin(\rho_n)\tan(\varphi_d)) \tag{5-22}$$

$$\xi = \arcsin(\cos(\rho_n)\sin(\varphi_d)) \tag{5-23}$$

The squint's dynamical range over the whole elevation angle range $\rho \in [\rho_{min}, \rho_{max}]$ is then given by

$$\varphi = \arcsin(\sin(\rho_i)\sin(\psi) + \cos(\rho_i)\sin(\xi)\cos(\psi)) \tag{5-24}$$

where

$$\rho_i = \arctan\left\{\frac{\tan(\rho)\cos(\xi) + \sin(\xi)\sin(\psi)}{cos(\psi)}\right\} \tag{5-25}$$

The squinted azimuth beamwidth $\Delta\varphi$ remains constant (in good approximation) if the optimum yaw and pitch values are selected, yet the azimuth bandwidth B_{az} decreases with the cosine of the squint:

$$B_{az}(\varphi) = \frac{2v\Delta\varphi\cos(\varphi)}{\lambda} = B_{az,0}\cdot\cos(\varphi) \tag{5-26}$$

where $B_{az,0}$ = Doppler bandwidth for the unsquinted case. Accordingly, for a squint angle of 45° we obtain a decrease in azimuth bandwidth (and hence, azimuth resolution) by roughly 30 %.

Another issue of squint mode acquisition is that for a given swath width to be illuminated, the time reserved for echo reception increases with squint. Since the echo reception has to fit into the time between two pulse transmissions, a trade-off between PRF and swath width has to be found.

5.4.1.4. Properties of Moving Targets

SAR images of moving targets suffer from the well-known *train-off-the-track* effect: any velocity component towards the sensor implies an additional Doppler shift, which in turn leads to a positional shift in the azimuth direction. This displacement can be evaluated exploiting Eq. 5-18, which establishes the relationship between Doppler shift and azimuth displacement of a (stationary) target. Rewriting the right side of Eq. 5-18 to

$$\frac{2\,\vec{v}_{rel}\cdot\vec{e}_R}{\lambda} = \frac{2\,v_{rel}\,\sin\varphi}{\lambda} \simeq \frac{2\,v_{Sat}}{\lambda}\frac{x}{R} \tag{5-27}$$

where v_{Sat} = satellite speed, R = sensor-to-target distance, x = off-broadside distance of the target, φ = off-broadside angle of the target, it immediately can be seen that an additional radial velocity component Δv is equivalent to an azimuth shift Δx with magnitude

$$\Delta x = \frac{\Delta v}{v_{Sat}}R \tag{5-28}$$

Consequently, any moving target with radial component encounters an azimuthal displacement in the slant-range image. This important feature inherent to all SAR observations has to be compensated by final remapping of the image pixels, taking advantage of either a priori knowledge of the scatterer's velocities or by exploiting ATI information.

5.4.2. Interferometric Processing

Interferometric processing includes the processing steps necessary to form an interferogram from two SLCs which contains the phase information suitably prepared for the specific application. In Fig. 5-9 the basic processing chain is depicted.

In the following, the steps *co-registration*, *interferogram noise filtering*, and *phase unwrapping* are discussed with respect to oceanic applications.

5.4.2.1. Co-Registration

Image co-registration is a smooth process for normal stripmap SAR data, but is much more challenging in the presence of high squint angles [*Bara et al.*, 2000]. A squinted imaging geometry introduces a phase ramp along a point target's impulse response function. Consequently, if both SLCs are misregistrated, an interferometric phase bias is caused. The dependence between phase bias $\Delta\phi$ and misregistration Δr is given by [*Bara et al.*, 2000]

$$\Delta\phi = \frac{4\pi}{\lambda}\Delta r(1 - \cos\varphi) \tag{5-29}$$

and is visualised in Fig. 5-10, where the maximum allowed co-registration error is plotted against the squint angle for given values of the phase error $\Delta\phi$. This simulation shows that especially for large squint angles (as proposed for Dual-Beam ATI) high demands on the co-registration accuracy are made. As an example, for 45° squint angle a phase error of more than 5° is caused by a misregistration of only 0.001 resolution cells. For the investigated bistatic system with its effective squint of around 2° and an assumed maximum allowable phase error of 5° we obtain a required co-registration accuracy of only 0.4 resolution cells, as already stated in Sec. 5.3.2.1..

Accurate co-registration can be achieved either by applying advanced correlation techniques like the spectral diversity method [*Scheiber & Moreira*, 2000] or by exploiting the knowledge of the terrain elevation, which enables the execution of a theoretical co-registration based on pure geometric calculations. The latter procedure is applicable especially for oceanic applications where the terrain information a priori is known precisely. The achievable accuracy of the spectral diversity method is reported in *Scheiber & Moreira* [2000] as 0.007 samples for ERS-1/2 data. The accuracy of the theoretical registration technique is dominated by potential terrain elevation errors. Fig. 5-11 shows results of a simulation about the impact of elevation errors on the registration accuracy. The calculations have been carried out for the X-band situation (cf. Tab. 5-1) and different cross-track baseline components $B_\perp$ (note, that the cross-track component is the predominant part, the along-track component causes a misregistration only for high squint angles, which is even then negligibly small). It can be read from Fig. 5-11 that only for large baselines the registration error becomes prominent, whereas for the typically small ATI values for $B_\perp$ the effect is negligible.

5.4.2.2. Noise Filtering

SAR interferograms may suffer from phase noise for a number of reasons. Amongst the most significant ones especially for ATI, the following three can be identified:

- *low SNR of the SAR data:* over water surfaces, low SNR is mainly caused by large incidence angles or, e.g. as an effect of low wind speeds, by lack of sufficient surface roughness (cf. Fig. 5-6).
- *temporal decorrelation of interferometric data:* due to changes of the illuminated surface between both observations (cf. ocean decorrelation time, Eq. 5-17).
- *Doppler spectra mismatch:* caused by different azimuth observation angles. As discussed in Sec. 5.3.2.1., this is only relevant for specific ATI configurations like the bistatic Cartwheel proposal.

The coherence images in Fig. 5-5 qualitatively illustrate correlation loss due to SNR and temporal decorrelation. A coherence drop can be identified from near to far range (left to right part of the images, caused by decreasing SNR) as well as from short to long timelags (lower image to upper image).

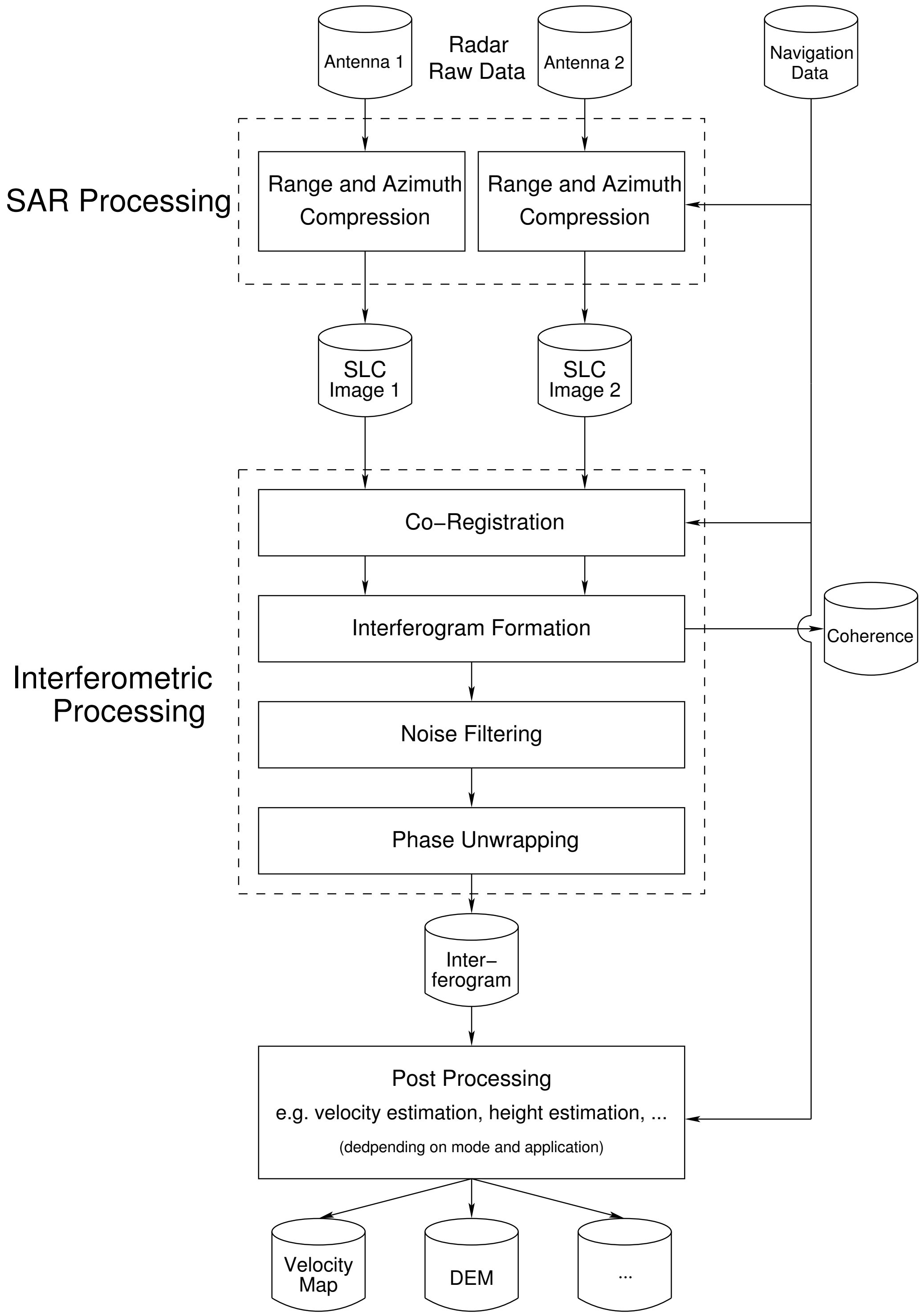

Figure 5-9: SAR and InSAR processing chain

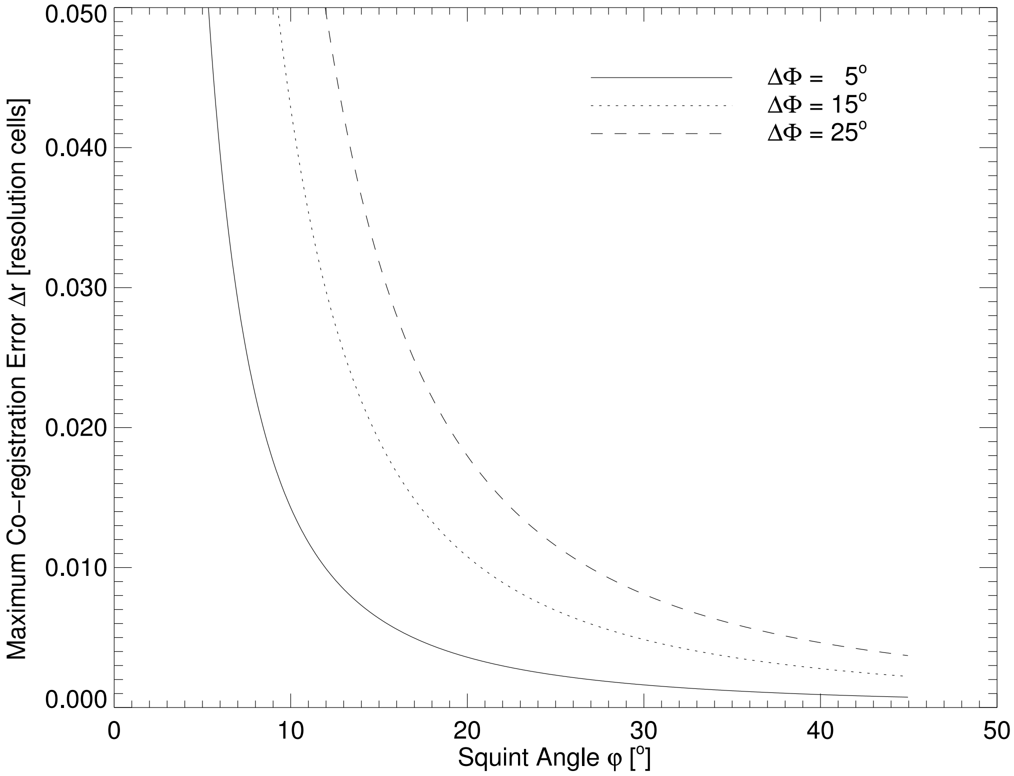

Figure 5-10: Maximum allowed co-registration error for given interferometric phase error $\Delta\phi$ as a function of squint angle

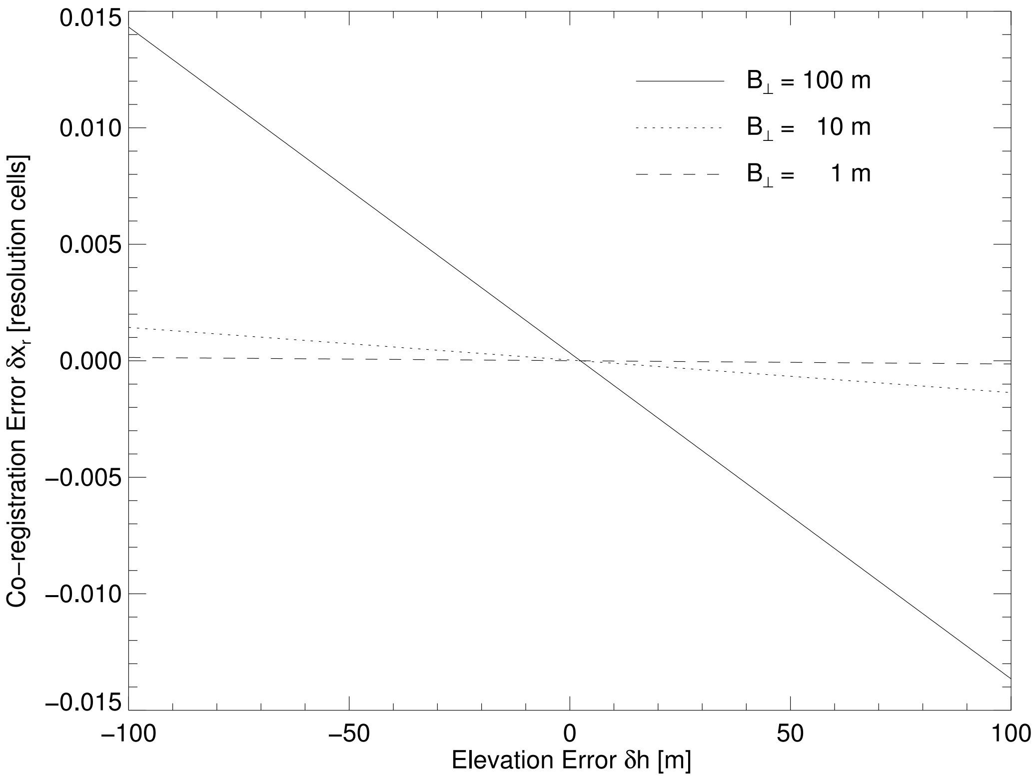

Figure 5-11: Co-registration error in range as a function of terrain elevation error for different effective cross-track baselines

All of the aforementioned error sources are of statistical nature, i.e. the introduced noise can be considered as "white". A common technique to reduce the phase standard deviation caused by that noise is the so-called "interferogram multilooking", a spatial averaging of the complex interferogram samples. In Fig. 5-4 the noise reduction effect for different numbers of looks N_L as a function of the inherent data coherence is displayed. As can be seen, the phase standard deviation can be reduced significantly by increasing N_L, yet the data coherence itself remains a dominating factor. Interestingly, noise reduction can be more effective than given by the $1/\sqrt{N_L}$ law, which has its reason in the interdependence between interferogram phase and amplitude: samples with higher amplitude generally tend to be closer to the expectation value than low amplitude samples. Interferogram phase statistics is investigated in full detail e.g. in *Just & Bamler* [1994] and *Lee et al.* [1994].

Signal filtering in general comes along with certain drawbacks. Since on principle filtering is a band-limiting process, it always reduces the geometric resolution of the data, therefore a proper trade-off between filtering strength and loss of resolution has to be found. Furthermore, any filtering should always try to avoid a degradation of the useful signal which carries the information to be extracted. Therefore, techniques adapted to the local shape of the signal spectrum are often advantageous over simple non-adaptive procedures like multilooking. As an example, adapting the filter strength to data coherence as proposed in *Goldstein & Werner* [1998] has given promising results when applied to airborne X-band ATI data [*Hirsch*, 2002]. Fig. 5-12 gives an impression of the corresponding filtering effect.

As a conclusion and design recommendation with respect to noise reduction, an ATI system should first of all minimise coherence loss by avoiding low SNR and large time lags. However, since a certain coherence loss is always present due to the nature of the imaging process, a system should be designed with sufficient resolution so that required noise filtering (with its resolution-degrading properties) still results in a dataset with the desired final resolution.

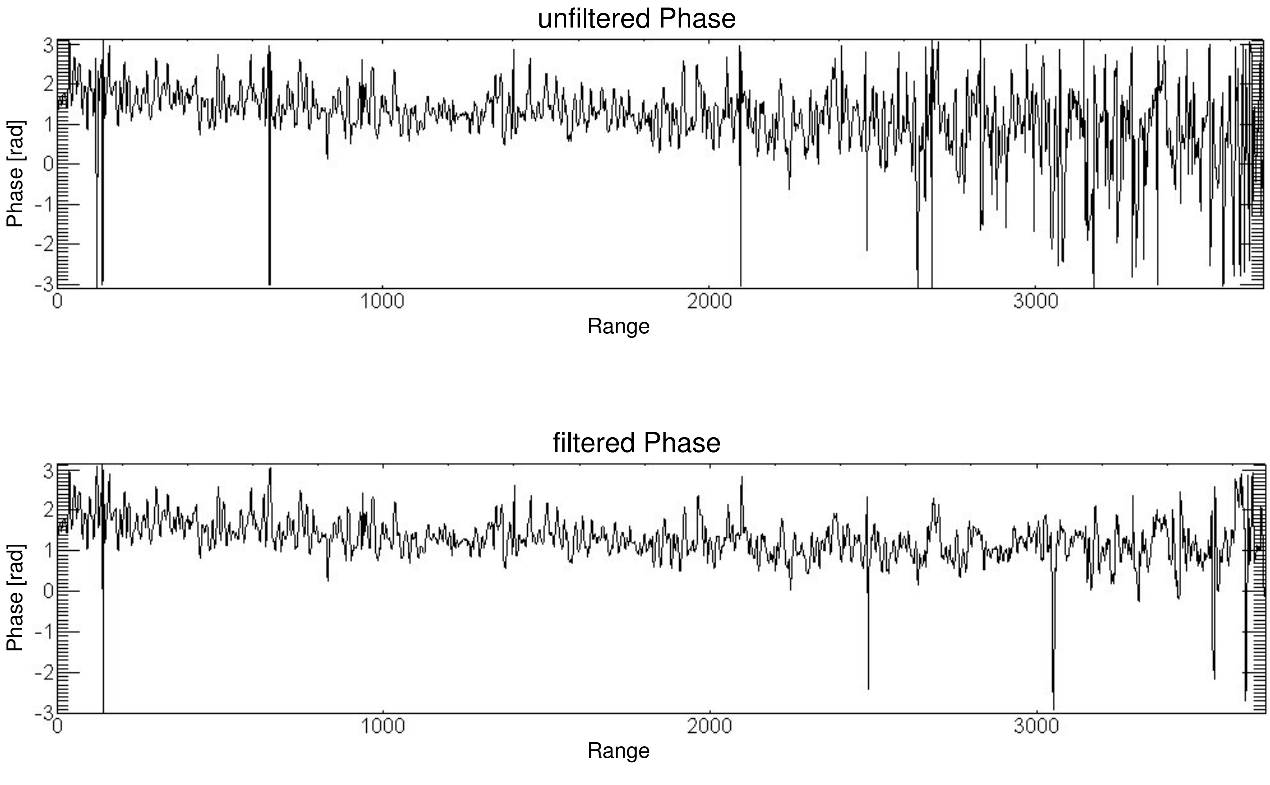

Figure 5-12: ATI phase unfiltered (upper part) and filtered with coherence adaptive filter (lower part). Data stem from an airborne X-band ATI acquisition over the North Sea near the island of Heligoland, Germany.

5.4.2.3. Phase Unwrapping

Phase unwrapping, defined as the process to resolve the 2π ambiguities in an interferogram, is necessary if the dynamical range of the observable (e.g. interferometric velocity) is greater than what can be covered with the range of phases $\phi \in [-\pi, \pi[$. Generally, an ATI system is designed such that the full range of expected velocities falls into the $[-\pi, \pi[$ interval. In this case, an absolute phase calibration becomes superfluous, which often is advantageous since in general, absolute calibration can be accomplished easily and reliably only if extended stationary targets (like coastal areas) are present in the scene. However, even with proper ATI design regarding the dynamical range, phase wraps may occur due to system noise or local anomalies of the observable, although fortunately those phase wraps are mostly restricted to ± 1 phase cycle.

Phase unwrapping of interferograms is problematic when data coherence drops due to interferometric phase noise or undersampling. For ATI data only phase noise is an important error source, which is caused by effects discussed in the previous Sec. 5.4.2.2.*. The phase unwrapping techniques currently in use (and still being developed) may be classified in mainly two categories, the *branch-cut* or *path-following* methods and the *least-squares estimation* methods [*Ghiglia & Pritt*, 1998; *Bamler & Hartl*, 1998]. No obvious preference for one or the other technique can be stated, however especially for ATI data with their almost exclusive restriction to ambiguities of ± 1 cycle additional plausibility checks can be introduced in order to avoid or remove 2π phase discontinuities. A corresponding technique based on morphological operations is described in *Hirsch* [2002].

5.4.3. Separation of ATI and XTI Contributions

In case of existence of along-track and cross-track components in the interferometric baseline both topography and surface motion contribute to the interferometric phase. As indicated in Eq. 5-21 cross-track and along-track phases add together. To separate both parts one needs at least two measurements undertaken with different baselines. This leads to a system of linear equations which can be solved. The measurements themselves can be achieved either using single-pass sensors in a certain orbit constellation (e.g. Cartwheel with one master satellite and two slave satellites) or by using a three-antenna system, as has been demonstrated in airborne campaigns [*Siegmund*, 2002].

One has to consider that especially contributions to the ATI phase are manifold, and therefore a separation of the phase components as well as the derivation of individual oceanographic parameters (like wave fields, surface currents) is difficult. Wind measurements and a highly accurate estimation of the topographic component are needed. A detailed study on combined ATI/XTI for oceanic applications, based on airborne data, has been carried out by *Siegmund* [2002].

It is useful to keep in mind that a true separation of ATI and XTI components is not always necessary for reasonable interpretation of combined ATI/XTI data. In many cases, a priori knowledge of physical phenomena enables the extraction of the desired parameter even from composite interferometric phase.

5.4.4. Geocoding

Geocoding of interferograms for oceanic applications is noteworthy for the following two reasons:

- geocoding of any spaceborne SAR image requires precise terrain elevation information due to the side-looking characteristics of the imaging geometry. An elevation error δh transforms directly into a positioning error δx depending on the incidence angle θ:

$$\delta x = \frac{\delta h}{\tan\theta} \tag{5-30}$$

  However, since the terrain elevation of ocean surfaces a priori is known to a decimeter (or, at the worst, meter) scale, the geocoding process in principle is accurately realisable.

- displacement of moving objects (cf. Sec. 5.4.1.4.), if not compensated through data remapping by exploiting a priori knowledge of the target's speed, is directly transformed into a positional error in the

* Undersampling is very unlikely if the system is designed to measure the expected observable's dynamical range with one phase cycle

final geocoded image. As an example, objects travelling with 1 m/sec velocity towards the sensor are subject to an azimuth displacement of 88 m (Eq. 5-28, parameters from Tab. 5-1).

5.4.5. Accuracy Requirements

According to the interferometric operating mode, the parameter extraction accuracy imposes requirements on the accuracy of certain system parameters. It has to be distinguished between ATI and XTI mode with their principal parameters interferometric velocity and terrain elevation, respectively.

ATI Based on Eq. 5-16 the contributions of the individual errors δv_{Sat}, $\delta\phi$, and $\delta B_{\|}$ to the total error for the interferometric velocity, δv, can be expressed by the following equations (bistatic case):

$$\begin{aligned} \delta v_{(v_{Sat})} &= -\frac{\lambda\phi}{2\pi B_{\|}} \cdot \delta v_{Sat} \\ \delta v_{(\phi)} &= -\frac{\lambda v_{Sat}}{2\pi B_{\|}} \cdot \delta\phi \\ \delta v_{(B_{\|})} &= \frac{\lambda\phi v_{Sat}}{2\pi B_{\|}^2} \cdot \delta B_{\|} \end{aligned} \tag{5-31}$$

Assuming a reasonable accuracy requirement for each component of 0.05 m/sec and a typical expected velocity of 1 m/sec, we obtain the following individual error constraints (X-band case):

$$\begin{aligned} \delta v_{Sat} &< 350\, m/sec \\ \delta\phi &< 12^\circ \\ \delta B_{\|} &< 7\, m \end{aligned} \tag{5-32}$$

The requirement for $\delta B_{\|}$ imposes an additional requirement on the platform attitude accuracy of single-pass systems. The main effect arises from an uncompensated yaw angle error $\delta\xi$ according to

$$\delta B_{\|} = B_{\|}\left(1 - \cos(\delta\xi)\right) \tag{5-33}$$

leading to a maximum allowable yaw angle error of 18°. Note that this value is more of theoretical use since it would require a single-pass system with 147 m baseline.

XTI Based on Eq. 5-3 the contributions of the individual errors δR, $\delta\phi$, and $\delta B_{\perp}$ to the total error for the terrain elevation, δh, can be expressed by the following equations (bistatic case):

$$\begin{aligned} \delta h_{(R)} &= \frac{\lambda\phi\sin\theta}{2\pi B_{\perp}} \cdot \delta R \\ \delta h_{(\phi)} &= \frac{\lambda R\sin\theta}{2\pi B_{\perp}} \cdot \delta\phi \\ \delta h_{(B_{\perp})} &= -\frac{\lambda R\phi\sin\theta}{2\pi B_{\perp}^2} \cdot \delta B_{\perp} \end{aligned} \tag{5-34}$$

Similar to the ATI case, the requirements for the corresponding parameters can be evaluated if a certain accuracy requirement for h is assumed*.

*However, within the scope of this chapter only ATI design considerations are investigated

5.5. Summary and Conclusions on Technical Issues

In this concluding section the main findings and recommendations related to technical issues discussed in this chapter are summarised. The section is divided into the main categories *Hardware*, *Data Acquisition*, and *Data Processing* and concludes with a discussion on the expected system performance of the assumed bistatic system.

Hardware

- The physical dimensions such as size and weight have to be designed as trade-off between system performance and costs.
- The orbit configuration/constellation design has to be adapted to the specific type of application. For ATI or combined ATI/XTI experiments an orbital design as proposed for the interferometric Pendulum rather than that for Cartwheel is recommended due to its constant along-track baseline.
- In general, radar hardware has to be designed in order to meet the system performance requirements.

Data Acquisition

- As SAR acquisition mode the conventional stripmap mode is most favourable due to its feature of supplying extended area coverage in short time periods. For a single-pass system with fixed baseline also the ScanSAR acquisition mode is advantageous due to its wide swath capability.
- Combined ATI/XTI is in principle a promising technique, but it requires at least one more observation (as compared to conventional InSAR).
- Dual-Beam ATI is in principle a promising technique as well, but demanding and cost-intensive from the hardware and processing point of view.

Data Processing

- SAR focusing for conventional stripmap data may be carried out with any of the proposed techniques *range/Doppler*, ω-*k*, and *chirp scaling*. Squint mode data preferably should be processed with one of the latter two techniques.
- Interferometric processing of data over ocean areas is in general straightforward since main issues of common InSAR such as layover/shadowing or other terrain-dependent effects (e.g. misregistration due to wrong topography) are only of minor importance. However, in case of highly squinted data high demands on accurate co-registration are made.
- For accurate geo-localisation, a remapping procedure for moving targets (like the ocean surface) has to be carried out.

Performance The derived performance values of the assumed bistatic InSAR system are summarised in the following Tab. 5-4. Together with the input parameters of Tab. 5-1 they define the overall performance of the system. In general, those parameters describe, from the technical point of view, a reasonable and realisable spaceborne interferometric SAR system for oceanic applications. In particular, all accuracy requirements can be met with current state-of-the-art radar and processing technology.

However, the investigated system may not be optimised for specific oceanic applications since the system it is based on (*TerraSAR*) has been designed primarily for land applications. As an example, the high ground resolution in X-band (1 m) is far too high for most of the oceanic problems. Even better performance might be possible with an exclusive design for ocean applications.

Table 5-4: Performance values for potential bistatic X- and L-band spaceborne systems based on system parameters of Tab. 5-1

Parameter	X-band	L-band
expected SNR for σ^0 = -10 dB and mid-swath	18 dB	26 dB
XTI critical baseline	12.8 km	13.8 km
proposed ATI timelag	10.5 msec	35 msec
proposed ATI baseline	147 m	490 m
ATI velocity resolution	0.05 m/sec	0.09 m/sec
interferometric phase noise for 20 interferometric looks, based on SNR and temporal decorrelation only	11°	10°
nominal absolute Doppler centroid f_{DC}	14.6 kHz	2.3 kHz
nominal f_{DC} difference	54 Hz	28 Hz
required co-registration accuracy due to squinted geometry	0.4 resol. cells	0.5 resol. cells
azimuth displacement of targets moving with 1 m/sec speed in line of sight	88 m	88 m
required accuracy for satellite velocity estimation	350 m/sec	180 m/sec
required accuracy for along-track baseline estimation	7 m	12 m
required accuracy for yaw angle estimation (single-pass only)	18°	13°

Acknowledgements

The images and data shown in Figs. 5-5 and 5-7 have been acquired within the *EuroROSE* project, which was funded by the European Commission under grant no. MAS3CT980168.

Data of Fig. 5-12 have been acquired within the *EURoPAK* experiment, which was financed by the German Federal Ministry of Education and Research (BMBF) through the German Aerospace Centre (DLR), Bonn, under grant no. 50 EE 9723.

List of Symbols

λ	radar wavelength
R	radar-to-target distance
h	terrain height
X_r	swath width
$B_\perp$	baseline perpendicular to look direction
$B_\parallel$	baseline parallel to look direction
α	platform roll angle
ψ	platform pitch angle
ξ	platform yaw angle
ζ	off-nadir baseline angle
φ	antenna squint angle
θ	antenna look angle
ρ	antenna elevation angle
θ_i	incidence angle
L_{el}	antenna height
L_{az}	antenna length
θ_{az}	antenna beamwidth in azimuth
B_{az}	system bandwidth in azimuth
B_r	system bandwidth in range
B_e	equivalent system bandwidth in range
P_t	transmitted power
P_r	received power
P_n	noise power
G	antenna gain
k	Boltzmann's constant
T	receiver temperature
F	receiver noise figure
L	system losses
ΔE	projected pulse length
h_{Sat}	satellite orbital height
v_{Sat}	satellite velocity
v_{rel}	relative velocity between sensor and target
c	speed of light
Δx_{az}	azimuth resolution
Δx_r	range resolution
σ_ϕ	interferometric phase noise
N_L	number of interferometric looks
σ	radar cross section
σ^0	normalised radar cross section
ϕ	interferometric phase
v	interferometric velocity
τ_s	ocean decorrelation time
γ	interferometric coherence
f_D	Doppler frequency
f_{DC}	Doppler centroid frequency

List of Abbreviations

AeS-1	airborne interferometric radar system of Aero-Sensing Radarsysteme GmbH
ATI	along-track interferometry
ERS-1/2	European remote sensing satellites
GPS	global positioning system
InSAR	interferometric synthetic aperture radar
IRU	inertial reference unit
NESZ	noise-equivalent sigma zero
PBW	processed (azimuth) bandwidth
PRF	pulse repetition frequency
rx	receiving (antenna)
SAR	synthetic aperture radar
SLC	single-look complex dataset
SNR	signal-to-noise ratio
SRTM	shuttle radar topography mission
tx	transmitting (antenna)
XTI	cross-track interferometry

References

Bamler, R., D. Geudtner, B. Schättler, P. Vachon, U. Steinbrecher, J. Holzner, J. Mittermayer, H. Breit, A. Moreira. RADARSAT ScanSAR interferometry. In: *Proceedings of IGARSS'99*, pp. 1517–1521. Hamburg [1999].

Bamler, R., P. Hartl. Synthetic aperture radar interferometry. *Inverse Problems*, 14, pp. R1–R54 [1998].

Bao, M., J. Schulz-Stellenfleth, S. Lehner, M. Eineder. First results on ocean wave imaging from the shuttle radar topography mission (SRTM). In: *Proceedings of IGARSS'01*, pp. 584–586. Sydney [2001].

Bara, M., R. Scheiber, A. Broquetas, A. Moreira. Interferometric SAR signal analysis in the presence of squint. *IEEE Trans. on Geoscience and Remote Sensing*, 38, no. 5, pp. 2164–2178 [2000].

Carrara, W. G., R. S. Goodman, R. M. Majewski. *Spolight synthetic aperture radar: signal processing algorithms*. Artech House [1995].

Curlander, J. C., R. N. McDonough. *Synthetic Aperture Radar Systems and Signal Processing*. Wiley Series in Remote Sensing. John Wiley & Sons [1991].

Davidson, G. W., I. Cumming. Signal properties of spaceborne squint-mode SAR. *IEEE Trans. on Geoscience and Remote Sensing*, 35, no. 3, pp. 611–617 [1997].

Eineder, M., R. Bamler, N. Adam, S. Suchandt, H. Breit, U. Steinbrecher, B. Rabus, W. Knöpfle. Analysis of SRTM interferometric X-band data: First results. In: *Proceedings of IGARSS'00*, pp. 2593–2595. Hawaii [2000].

Elachi, C. *Spaceborne Radar Remote Sensing: Applications and Techniques*. IEEE Press [1988].

Franceschetti, G., R. Lanari. *Synthetic Aperture Radar Processing*. CRC Press [1999].

Frasier, S. J., A. J. Camps. Dual-beam interferometry for ocean surface current vector mapping. *IEEE Trans. on Geoscience and Remote Sensing*, 39, no. 2, pp. 401–414 [2001].

Gatelli, F., A. M. Guarnieri, F. Parizzi, P. Pasquali, C. Prati, F. Rocca. The wavenumber shift in SAR interferometry. *IEEE Trans. on Geoscience and Remote Sensing*, 32, no. 4, pp. 855–865 [1994].

Ghiglia, D. C., M. D. Pritt. *Two-dimensional Phase Unwrapping – Theory, Algorithms, and Software*. John Wiley & Sons [1998].

Goldstein, R. M., C. L. Werner. Radar interferogram filtering for geophysical applications. *Geophysical Research Letters*, 25, no. 21, pp. 4035–4038 [1998].

Greidanus, H., E. Huising, Y. Platschorre, R. V. Bree, D. V. Halsema, E. Vaessen. Coastal currents with along-track interferometry. In: *Proceedings of IGARSS'99*, pp. 2607–2609. Hamburg [1999a].

—. Coastal DEMs with cross-track interferometry. In: *Proceedings of IGARSS'99*, pp. 2161–2163. Hamburg [1999b].

Hirsch, O. Neue Verarbeitungsverfahren von Along-Track Interferometrie Daten eines Radars mit synthetischer Apertur [2002]. Submitted as PhD thesis, Universität Siegen, Germany.

Jin, M. Y., C. Wu. A SAR correlation algorithm which accomodates large range migration. *IEEE Trans. on Geoscience and Remote Sensing*, 22, pp. 592–597 [1984].

Just, D., R. Bamler. Phase statistics of interferograms with applications to synthetic aperture radar. *Applied Optics*, 33, no. 20, pp. 4361–4368 [1994].

Lee, J.-S., K. W. Hoppel, S. A. Mango, A. R. Miller. Intensity and phase statistics of multilook polarimetric and interferometric SAR imagery. *IEEE Trans. on Geoscience and Remote Sensing*, 32, pp. 1017–1028 [1994].

Mittermayer, J., G. Krieger, M. Wendler, A. Moreira, E. Thouvenot, T. Amoit, R. Bamler. Interferometric performance estimation for the interferometric Cartwheel in combination with a transmitting SAR-satellite. In: *Proceedings of IGARSS'2001*, pp. 2955–2957. Sydney [2001].

Moore, R. K., J. P. Claassen, Y. H. Lin. Scanning spaceborne synthetic aperture radar with integrated radiometer. *IEEE Trans. on Aerospace and Electronic Systems*, 17, pp. 410–420 [1981].

Moreira, A., G. Krieger, J. Mittermayer. Comparison of several bi-static SAR configurations for spaceborne SAR interferometry [2001]. Oral presentation at *IGARSS'01* symposium, Sydney.

Moreira, J. *Bewegungsextraktionsverfahren für Radar mit synthetischer Apertur*. DLR technical report FB 92-31, Technische Universität München [1992].

Raney, R. K., H. Runge, R. Bamler, I. G. Cumming, F. H. Wong. Precision SAR processing using chirp scaling. *IEEE Trans. on Geoscience and Remote Sensing*, 32, no. 4, pp. 786–799 [1994].

Scharroo, R. ERS-1 operational orbit determination. In: E. Wisse, M. C. Naeije, R. Scharroo (Eds.), *Processing of ERS-1 and TOPEX/Poseidon Altimeter Measurements*, number 93-11 in BCRS report. Netherlands Remote Sensing Board [1993].

Scheiber, R., A. Moreira. Coregistration of interferometric SAR images using spectral diversity. *IEEE Trans. on Geoscience and Remote Sensing*, 38, no. 5, pp. 2179–2191 [2000].

Schulz-Stellenfleth, J., J. Horstmann, S. Lehner, W. Rosenthal. Sea surface imaging with an across-track interferometric synthetic aperture radar: The SINEWAVE experiment. *IEEE Trans. on Geoscience and Remote Sensing*, 39, no. 9, pp. 2017–2018 [2001].

Schwäbisch, M., D. Geudtner. Improvement of phase and coherence map quality using azimuth prefiltering: Examples from ERS-1 and X-SAR. In: *Proceedings of IGARSS'95*, pp. 205–207. Firenze, Italy [1995].

Siegmund, R. Bestimmung von topographischen und hydrologischen Parametern im Wattenmeergebiet mittels SAR-Interferometrie [2002]. Submitted as PhD thesis, Christian-Albrechts-Universität Kiel, Germany.

Skolnik, M. I. (Ed.). *Radar Handbook*. McGraw-Hill, second edition [1990].

Soumekh, M. *Synthetic Aperture Radar Signal Processing*. Wiley & Sons [1999].